New Type of 2D Perovskites with Alternating Cations in the Interlayer Space, (C(NH 2) 3)(CH 3 NH 3) n Pb n I 3 n +1 : Structure, Properties, and Photovoltaic Performance

Chan Myae Myae Soe, Constantinos C Stoumpos, Mikaël Kepenekian, Boubacar Traoré, Hsinhan Tsai, Wanyi Nie, Binghao Wang, Claudine Katan, Ram Seshadri, Aditya D Mohite, et al.

New Type of 2D Perovskites with Alternating Cations in the Interlayer Space, $(C(NH_2)_3)(CH_3NH_3)_nPb_nI_{3n+1}$: Structure, Properties and Photovoltaic Performance

Chan Myae Myae Soe,[1#] Constantinos C. Stoumpos,[1#] Mikaël Kepenekian,[2] Boubacar Traoré,[2] Hsinhan Tsai,[3] Wanyi Nie,[3] Binghao Wang,[1] Claudine Katan,[2] Ram Seshadri,[4,5,6] Aditya D. Mohite,[3] Jacky Even,[7] Tobin J. Marks,[1] Mercouri G. Kanatzidis[1]*

[1]Department of Chemistry and Argonne-Northwestern Solar Energy Research Center, Northwestern University, Evanston, Illinois 60208, USA

[2]Institut des Sciences Chimiques de Rennes (ISCR), UMR 6226, CNRS - Université de Rennes 1 - Ecole Nationale Supérieure de Chimie de Rennes - INSA Rennes, France

[3]Los Alamos National Laboratory, Los Alamos, NM 87545, USA

[4]Materials Research Laboratory, University of California, Santa Barbara, California 93106, USA

[5]Materials Department, University of California, Santa Barbara, California 93106, USA

[6]Department of Chemistry and Biochemistry, University of California, Santa Barbara, California 93106, USA

[7] Fonctions Optiques pour les Technologies de l'Information (FOTON), UMR 6082, CNRS - INSA Rennes - Université de Rennes 1, France

*Corresponding authors. E-mail: m-kanatzidis@northwestern.edu

KEYWORDS: Layered compounds, perovskite photovoltaics, solvent-engineering, hot-casting, crystallinity

ABSTRACT

We present the new homologous series, $(C(NH_2)_3)(CH_3NH_3)_nPb_nI_{3n+1}$ (n = 1, 2, 3), of layered 2D perovskites. Structural characterization by single-crystal X-ray diffraction reveals that these compounds adopt an unprecedented structure type which is stabilized by the alternating ordering of the guanidinium and methylammonium cations in the interlayer space (ACI). Compared to the more common Ruddlesden-Popper (RP) 2D perovskites, the ACI perovskites have a different stacking motif and adopt a higher crystal symmetry. The higher symmetry of the ACI perovskites is expressed in its physical properties, which show a characteristic decrease of the bandgap with respect to their RP perovskite counterparts with the same perovskite layer thickness (n). The compounds show a monotonic decrease in the optical gap as n increases: E_g = 2.27 eV for n = 1 to E_g = 1.99 eV for n = 2 and E_g = 1.73 eV for n = 3, which show slightly narrower gaps compared to the corresponding RP perovskites. First-principles theoretical electronic structure calculations confirm the experimental optical gap trends suggesting that the ACI perovskites are direct bandgap semiconductors with wide valence and conduction bandwidths. To assess the potential of the ACI perovskites towards solar cell applications, we studied the $(C(NH_2)_3)(CH_3NH_3)_3Pb_3I_{10}$ (n = 3) compound. Compact thin films from the $(C(NH_2)_3)(CH_3NH_3)_3Pb_3I_{10}$ compound with excellent surface coverage can be obtained from the anti-solvent dripping method. Planar photovoltaic devices from optimized ACI perovskite films yield a power-conversion-efficiency of 7.26% with a high open-circuit voltage of ~1 V and a striking fill factor of ~80%.

INTRODUCTION

Two-dimensional (2D) layered halide perovskites are highly promising candidates for optoelectronic applications, and this has sparked new investigations of these materials from the synthetic, physicochemical and applications point of view.[1-8] Unlike the more extensively studied three-dimensional (3D) AMX_3 perovskites (A^+ = Cs, CH_3NH_3 (MA) or $HC(NH_2)_2$ (FA)) where the possibility of a 3D stable crystal structure is limited by the size and shape of the A^+ cation[9-10] the lower-dimensional perovskite semiconductors offer a much higher degree of structural versatility and permit better control and fine-tuning of the optoelectronic properties.[11] Conceptually, upon "cutting" the 3D parent compound along a specific crystallographic plane, infinite nanosheets with a slab thickness of atomic or molecular size can be obtained, which are separated by organic cations acting as spacers and in this context, they can be considered as natural quantum wells (QWs). These ultrathin negatively charged perovskite nanosheets are held together by intercalating organic cations, which balance the charge and support the structural integrity of the 2D perovskites. Depending on the cut in the 3D framework, the 2D perovskites can be subcategorized as <100>, <110>, and <111>-oriented perovskites. What effectively determines this crystallographic cut is the size and shape of the spacer cation. Cations employed for this purpose to date include, but not limited to, ammonium,[1, 6, 12-15] amidinium,[16-17] imidazolium[18] and phosphonium[19] ions. Among the <100> perovskites, the Ruddlesden-Popper (RP) perovskites,[20-21] are by far the most common structural type with less common types being the Dion-Jacobson (DJ),[22-23] and Aurivillius (AV)[24-26] phases both of which finding paradigms only in oxide perovskite families. The less common DJ phases are chemically different from the RP phases in that the two spacer cations $(M)_2$ of the $(M)_2A_{n-1}B_nO_{3n+1}$ RP structure are replaced by

a single alkali metal M' spacer in the $M'A_{n-1}B_nO_{3n+1}$ DJ structure. The AV perovskites have a closer relationship to the RP compounds, but they are distinctively different because the individual M cations are replaced by extended cationic $[(Bi_2O_2)^{2+}]_\infty$ layers, which drastically change the physical properties of the compounds.[27-28] From the crystallographic viewpoint, the DJ phases are accompanied by a relative shift of the layers along the *ab*-plane (½ , 0 shift, $KLaNb_2O_7$-type) [29] or no shift at all (0, 0 shift, $CsLaNb_2O_7$-type)[30] in the perovskite layers, contrary to the RP phases that universally exhibit a (½, ½) shift. The (½, 0) case results in an 'eclipsed' configuration of the layers along the stacking direction. The structural chemistry of the DJ oxide perovskites has recently undergone a resurgence after the predictions that such structures can exhibit ferroelectricity[31-32] using certain material design principles.[33] Despite the abundance of DJ perovskites in oxides,[34] this structural type is hitherto unknown in the hybrid halide perovskites.

Herein we report on the $(C(NH_2)_3)(CH_3NH_3)_nPb_nI_{3n+1}$ (n = 1-3) family of 2D perovskites, new type of 2D halide perovskite which feature two different alternating cations in the interlayer space (ACI). This results is cation-ordering in the interlayer space with the two spacer cations being guanidinium ($C(NH_2)_3$, $GA)^+$ and methylammonium (CH_3NH_3), $MA)^+$. This unique ordering leads to the formation of an unprecedented structure type which blends the chemical formula of the RP perovskites with the structural features of the DJ perovskites. The ordering of the cations leads to a (½, 0) shift of the layers reminiscent of the DJ perovskites but at the same differing in the occupation of the interlayer sites due to charge balance restrictions, thus leading to a different centering of the unit cell (Table 1). GA was chosen as a spacer since it has a structural formula reminiscent of the formamidinium ($HC(NH_2)_2$, $FA)^+$ and iodoformamidinium ($IC(NH_2)_2$, $IFO)^+$ cations, which stabilize the perovskite structure, either in its 3D form[35] or in

the <110> 2D perovskite,[36] respectively. Conceptually, GA is obtained by substituting the C-H hydrogen atom in FA or C-I iodine atom in IFO with an -NH_2 group. The present study expands on the series of simple 2D guanidinium compounds that adopt the <110>-oriented RP perovskite type, originally obtained by Szafrański and coworkers[37-39] and recently revisited by the Hillebrecht's group.[40] The ACI perovskites reported in this work find join the very recently reported $GACs_nPb_nX_{3n+1}$ compounds which adopt a similar crystal structure.[41] Here the ACI phase $GAMA_nPb_nI_{3n+1}$ series (n = 1, 2 and 3) has been structurally characterized by means of single-crystal X-ray diffraction. The compounds exhibit lower bandgaps and slightly reduced photoluminescence (PL) intensity compared to the known Ruddlesden-Popper (RP) perovskites having butylammonium (BA) spacers. The observed trend in the bandgap within the ACI series can be captured by DFT calculations. They predict that ACI have slightly narrower (n = 1, 3) or comparable (n = 2) bandgap compared to the RP perovskites for their corresponding n-member. We also investigated the photovoltaic performance of the highest member of the series $GAMA_3Pb_3I_{10}$ (n = 3), which adopts the centrosymmetric *Imma* space group and has the smallest optical gap in the series, E_g = 1.73 eV, making it a good candidate for a light absorber material in both single-junction and tandem solar cells. Smooth, compact high-quality thin films were obtained by employing the solvent-engineering method with anti-solvent dripping at an optimized delay time. While the morphology improves drastically for the films before and after anti-solvent treatment, the crystallinity is found to remain unaffected. Planar solar cells comprising the optimized n = 3 films exhibit a promising power-conversion-efficiency (PCE) of 7.26% (average 6.69 ± 0.47%), with a high Voc of 0.974 V and an impressive fill factor (FF) of ~80%, which is the highest value reported for 2D perovskite solar cells.

EXPERIMENTAL

Materials. Lead oxide (PbO, 99%), methylamine hydrochloride (CH_3NH_3Cl, 99%), guanidine hydrochloride (($C(NH_2)_3Cl$, ≥ 98%), hydriodic acid (HI, 57 wt% in H_2O), hypophosphorous acid (H_3PO_2, 50 wt% in H_2O), N,N-dimethylformamide (DMF, anhydrous, 99.8%), dimethylsulfoxide (DMSO, anhydrous, ≥ 99.9%), and chlorobenzene (CB, anhydrous, 99.8%) were used as received from Sigma-Aldrich without further purification. Poly(3,4-ethylenedioxythiophene)-poly(styrenesulfonate) (PEDOT:PSS) and phenyl-C61-butyric acid methyl ester ($PC_{61}BM$, > 99%) were purchased from Clevios and American Dye Source Inc., respectively.

Materials Synthesis. *$((C(NH_2)_3)_2PbI_4$.* PbO (670 mg, 3 mmol) was dissolved in a mixture of 20.0 ml of aqueous HI and 1.7 ml of aqueous H_3PO_2 by heating to boiling under constant magnetic stirring for at least 15 min. To the hot bright yellow solution was added solid $C(NH_2)_3Cl$ (573 mg, 6 mmol), and the reaction was kept under constant heating and stirring for a few hours until ~25% of the acid solution has evaporated. The stirring was then discontinued, and the hot supersaturated solution was slowly quenched to room temperature. Bright yellow plate-like crystals precipitated after the solution was allowed to stand for 2 days. The crystals were isolated by suction filtration and thoroughly dried at 60 °C in a vacuum oven (Yield: 0.66g, 26% based on total Pb).

$(C(NH_2)_3)(CH_3NH_3)PbI_4$. PbO (670 mg, 3 mmol) was dissolved in a mixture of 20.0 ml of aqueous HI and 1.7 ml of aqueous H_3PO_2 by heating to boiling under constant magnetic stirring for at least 15 min. To the hot bright yellow solution were added solids CH_3NH_3Cl (203 mg, 3

mmol) and $C(NH_2)_3Cl$ (287 mg, 3 mmol), and the reaction was kept under constant heating and stirring for a few hours until ~25% of the acid solution has evaporated. The stirring was then discontinued, and as the hot supersaturated solution was slowly cooled to room temperature. Red crystals precipitated after the solution was allowed to stand for 2 days. The crystals were isolated by suction filtration and thoroughly dried at 60 °C in a vacuum oven (Yield: 0.54g, 22% based on total Pb).

$(C(NH_2)_3)(CH_3NH_3)_2Pb_2I_7$. PbO (2232 mg, 10 mmol) was dissolved in a mixture of 20.0 ml of aqueous HI and 1.7 ml of aqueous H_3PO_2 by heating to boiling under constant magnetic stirring for at least 15 min. To the hot bright yellow solution were added solids CH_3NH_3Cl (675 mg, 10 mmol) and $C(NH_2)_3Cl$ (478 mg, 5 mmol), and the reaction was kept under constant heating until all the the reactants dissolved. The stirring was then discontinued, and as the hot supersaturated solution was slowly quenched to room temperature, upon which the precipitation of dark red crystals commenced. The crystals were allowed to settle for further 2 h, before the crystals were isolated by suction filtration and thoroughly dried at 60 °C in a vacuum oven (Yield: 1.64g, 23% based on total Pb).

$(C(NH_2)_3)(CH_3NH_3)_3Pb_3I_{10}$. PbO (2232 mg, 10 mmol) was dissolved in a mixture of 20.0 ml of aqueous HI and 1.7 ml of aqueous H_3PO_2 by heating to boiling under constant magnetic stirring for at least 15 min. To the hot bright yellow solution were added solids CH_3NH_3Cl (675 mg, 10 mmol) and $C(NH_2)_3Cl$ (318 mg, 3.33 mmol), and the reaction was kept under constant heating until all the the reactants dissolved. The stirring was then discontinued, and as the hot supersaturated solution was slowly quenched to room temperature, upon which the precipitation of black crystals commenced. The crystals were allowed to settle for further 2 h, before the

crystals were isolated by suction filtration and thoroughly dried at 60 °C in a vacuum oven (Yield: 1.50g, 22% based on total Pb).

Materials Characterization. High resolution synchrotron powder X-ray diffraction (SXRD) data were collected at beamline 11-BM-B of the Advanced Photon Source (APS), Argonne National Laboratory using $\lambda = 0.517040$ Å. Discrete detectors covering an angular range from 0 to 4º 2θ are scanned over a 26º 2θ range, with data points collected every 0.001º 2θ and a scan speed of 0. 1º/s.

Scanning Electron Microscopy (SEM) images of the perovskite crystals were obtained by using a Hitachi SU3400 equipped with an electron beam accelerated at 10-20 kV.

A Shimadzu UV-3600 PC double-beam, double-monochromator spectrophotometer was used to acquire room-temperature optical diffuse reflectance spectra of the powdered samples in the range of 200-2500 nm. $BaSO_4$ was used as a non-absorbing reflectance reference, and reflectance data were converted to absorbance data via Kubelka–Munk transformation.[42-44]

Photoluminescence spectra were collected on oriented crystals using Horiba LabRam Evolution high-resolution confocal Raman microscope spectrometer (600 g/mm diffraction grating) equipped with a diode CW laser (473 nm, 25 mW) and a Synapse CCD camera.

Single-crystal X-ray diffraction experiments were performed using a STOE IPDS II or IPDS 2T diffractometer with Mo Kα radiation ($\lambda = 0.71073$ Å) and operating at 50 kV and 40 mA. Integration and numerical absorption corrections were performed using the X-AREA, X-RED, and X-SHAPE programs. The structures were solved by charge flipping and refined by full-matrix least squares on F^2 using the Jana2006 package.[45] The PLATON software[46] was used to identify the twinning domains and validate the space groups of the compounds.

Theoretical calculations. First-principles calculations are based on density functional theory (DFT) as implemented in the Siesta package.[47] Calculations have been carried out with the GGA functional in the PBE form, using the experimentally determined crystal structures.[48] Spin-orbit coupling is taken into account through the on-site approximation as proposed by Fernández-Seivane *et al*.[49] Core electrons are described with Troullier-Martins pseudopotentials.[50] The valence wavefunction is developed over a double-ζ polarized basis set of finite-range numerical pseudoatomic orbitals.[51] An energy cutoff of 150 Ry for real-space mesh size is used as well as a 1×4×4 *k*-point sampling grid for sampling the Brillouin zone.

Thin Film Characterization. AFM images were acquired using a Dimensional Icon Scanning Probe Microscope (Veeco) in tapping mode. Powder X-ray diffraction measurements were carried out on a Rigaku MiniFlex600 X-ray diffractometer (Cu Kα radiation, λ = 1.5406 Å) operating at 40 kV and 15 mA. GIWAXS measurements were performed at Beamline 8-ID-E of the Advanced Photon Source (APS) at Argonne National Laboratory. Samples prepared on Si/PEDOT:PSS substrates were exposed to an X-ray beam (λ = 1.6868Å) at an incident angle of 0.20° for 5 s, and the scattered light was collected by a Pilatus 1 M pixel array detector at 204 mm from the sample. Absorbance data were collected on Cary 6000i UV-Vis-NIR spectrophotometer in the 175-1800 nm region.

Solar Cell Device Fabrication. The FTO-coated glass substrates (TEC7, 2.2 mm, Hartford Glass Co. Inc.) were cleaned by sequential sonication in aqueous detergent, deionized water, isopropanol (IPA), and acetone (ACE) for 15 min each, followed by a 5 min oxygen plasma treatment. A thin layer of PEDOT:PSS was deposited on the pre-cleaned FTO substrates by spin-coating at 6,000 rpm for 30 s and annealed at 150 °C for 30 min in air. The substrates were then transferred to a nitrogen-filled glove box to complete the rest of the device fabrication. Solutions

of $GAMA_3Pb_3I_{10}$ were prepared by dissolving 300 mg of the oven-dried crystals in 1 ml of DMF and 100 µl of DMSO solvents. For perovskite thickness study, various concentrations of the compound (20 mg, 25 mg, 30 mg, 35 mg, and 40 mg) in 100 µl:10 µl DMF:DMSO were used. The perovskite layer was deposited by spin-casting 60 µl of the as-prepared solution on the ITO/PEDOT:PSS substrates at 500 rpm. for 3s, followed by 4,000 rpm. for 60 s. For solvent-engineered films, 300 µl of CB anti-solvent was dropped on the spinning substrate at various delay times (3 s, 5 s, 10 s, 20 s, 30 s, 40 s, and 50 s), and the films turned brown instantaneously. The substrates were then annealed at 80 °C for 15 min to ensure removal of any remaining solvent residuals. $PC_{61}BM$ layer was deposited on the perovskite film from a 20 mg/ml $PC_{61}BM$ solution in CB at 5,000 rpm. for 30 s. Finally, 150 nm of Al was thermally evaporated through a shadow mask at a pressure of $\sim 2 \times 10^{-7}$ Torr. The active area of the device was 0.09 cm^2.

Solar Cell Device Characterization. The current density vs. voltage (J-V) characteristics were collected in air without any encapsulation using a Keithley 2400 source meter under simulated AM 1.5G irradiation (100 mW/cm^2) generated by a standard solar simulator (Abet Technologies). The light intensity was calibrated by using an NREL-certified monocrystalline Si reference cell to reduce the spectral mismatch.

RESULTS AND DISCUSSION

Materials synthesis. The synthesis of the series of $(C(NH_2)_3)_2PbI_4$ and $(C(NH_2)_3)(CH_3NH_3)_nPb_nI_{3n+1}$ compounds was accomplished by mixing stoichiometric ratios of pre-dried guanidinium chloride (GACl, $C(NH_2)_3Cl$), methylammonium chloride (MACl, CH_3NH_3Cl), and lead oxide (PbO) in a hot HI solution. As soon as the supersaturated, clear, bright yellow solution was removed from the hot plate and left to cool to ambient temperature, crystals of the title compounds started forming. Bright yellow plates of $(C(NH_2)_3)_2PbI_4$, red needles of $(C(NH_2)_3)(CH_3NH_3)PbI_4$, dark red needles of $(C(NH_2)_3)(CH_3NH_3)_2Pb_2I_7$, and black needles of $(C(NH_2)_3)(CH_3NH_3)_3Pb_3I_{10}$ were obtained, Figure 1. Unlike the RP perovskites, ACI perovskites obey a different synthetic protocol requiring a fully stoichiometric reaction in order to to crystallize in pure form. This is presumably because of the higher solubility of guanidinium salts in the reaction medium, in contrast to the long aliphatic ammonium cations used in the synthesis of the RP perovskites. The synthetic procedure finds an additional obstacle in the form of the reaction by-product the yellow $(C(NH_2)_3)PbI_3$,[37] a relatively insoluble one-dimensional (1D) "perovskitoid" of the NH_4CdCl_3 structure-type which competes with the precipitation of the ACI perovskite phases.[11] The co-formation of two reaction products was also observed in the Sn-based GA systems[11] with the 2D perovskite $(C(NH_2)_3)_2SnI_4$) being the kinetic reaction product

and the 3D ($(C(NH_2)_3)SnI_3$) perovskite being the thermodynamic product. However, in the case of the $(C(NH_2)_3)_2PbI_4$/$(C(NH_2)_3)PbI_3$ system this tendency inverts with the $(C(NH_2)_3)_2PbI_4$ being the thermodynamic product and $GAPbI_3$ the kinetic one, possibly due to the lower dimensionality of the 1D perovskitoid, which makes it easier to precipitate. With the hindsight of the behavior of the pure guanidinium systems, we conducted the reactions to synthesize the $(C(NH_2)_3)(CH_3NH_3)_nPb_nI_{3n+1}$ (n = 1-3) perovskites under relatively low concentrations below the saturation point of the solution, in order to avoid the formation of the 1D by-product.

All the ACI perovskites crystallize in high purity but their yield is relatively low (~25%) due to the special synthetic considerations discussed above, Figure 1b. An exception is found for $(C(NH_2)_3)(CH_3NH_3)PbI_4$ (the n = 1) member which shows a photo-instability (in solution and in the solid state) towards decomposition to the higher n = 2 member, presumably through a disproportionation mechanism. The photoreaction is not severe and it occurs only on the surface of the crystallites. A similar photosensitivity has been observed for the similar cation iodo-formamidinium cation n = 1 perovskite which degrades upon ambient light irradiation.[52] Another important characteristic of the ACI perovskites that differentiates them from the RP perovskites is their mechanical behavior. All ACI perovskites are brittle and tend to crack when mechanical force is applied, as opposed to the RP perovskites that are more malleable and tend to undergo a plastic deformation. As will be discussed below, the unique mechanical properties of the ACI perovskites arise from their tight, more 3D-like crystal structure, which locks the layers in place with respect to one another in contrast to the RP perovskites in which the floppy organic chains of the spacers lend the materials additional flexibility.

Description of the crystal structures. The crystal structures of the homologous ACI perovskite series, $(GA)(MA)_nPb_nI_{3n+1}$ (n = 1-3), are illustrated in Figure 2; selected crystallographic data are

presented in Table 2, and selected bonding parameters are provided in Table 3. All compounds crystallize in orthorhombic space groups with their unit cell dimensions being [a x 2a x 2(a·n+x)], where a ~ 6.3 Å is the lattice parameter of the idealized cubic 3D perovskite and x ~ 3.1 Å is the interlayer spacing (Table 2). The odd n-members (n = 1, n = 3) adopt the centrosymmetric *Imma* space group, whereas the even n-member (n = 2) adopts the polar noncentrosymmetric *Bmm*2 space group. The difference in odd and even members of homologous 2D perovskites series is expected as it arises from the changes in the crystallographic symmetry element that bisects the perovskite layers themselves along the *ab*-plane. For even n-members a mirror plane is present whereas for odd n-numbers this is replaced by a glide plane.[53] As a consequence of this trend all even-numbered halide 2D perovskites that bear MA as the "perovskitizer" cation tend to be noncentrosymmetric due to the incompatibility of the $CH_3NH_3^+$ cation of sitting on a mirror plane.[6, 54] Even though this assignment is ambiguous because of the dynamic disorder present in most of the halide perovskites,[55] strictly crystallographic criteria suggest the noncentrosymmetric structure to be the most favorable one.[56-57]

The crystal structures of the $(GA)(MA)_nPb_nI_{3n+1}$ ACI perovskites are unique among 2D perovskites because they are characterized by a very unusual ordering of the GA and MA cations which act as spacers between the perovskite layers. The GA/MA ordering leads to a doubling of the unit cell along the *b*-axis relative to the ideal undistorted cell, which coincides with the preferred growth direction of the crystals which adopt a needle-shaped morphology. The doubled *b*-axis hosts two individual $(PbI_6)^{4-}$ units, whereas the GA and MA cations form individual stacks along the crystallographic *a*-axis to engulf a single $(PbI_6)^{4-}$ unit. In order to accommodate the ordering of the spacers, the perovskite layers deviate from their idealized tetragonal symmetry,

undergoing a strong octahedral tilting along the cation ordering axis (*b*-axis). Each layer compresses to engulf the compact MA spacer and expands to allow the incorporation of the bulky GA cation at the layer edges, forming rhombic and hexagonal channels, respectively in the process, Figure 3. The other two dimensions of the perovskite, along the *a* and *c* axes, remain relatively undistorted as there is no mismatch in the crystal packing of the organic cations. The MA cations that reside within the cuboctahedral perovskite cavities inside the layer adopt their usual orientation, by aligning along the crystallographic c-axis in a very similar arrangement to that observed ion the 3D perovskite $MAPbI_3$.

In order to better highlight the special features of the ACI perovskites it is important to compare them with the common structure archetypes. The general distinctive features of the DJ perovskites over the RP perovskites are: i) the number of cations spanning the layers is reduced to one in DJ perovskites vs. two in the RP perovskites; ii) the change in the relative arrangement of two adjacent layers which in the case of the DJ perovskites involves a shift by half a unit cell in one direction (½, 0) or none at all (0, 0), but in RP perovskites involves a universal display of a half unit cell shift in both a and b crystallographic axes (½, ½).[58] In oxides, the crystal structure of DJ perovskites is strongly dependent on the size of the spacer cation and hinges between the two archetypes; the (0,0) modification (*P*4/*mmm* archetype) is obtained for large cations (Rb, Cs) which favor the occupation of the 8-coordinate sites between the layers, locking the layers on top of one another. Small cations (Li, Na) on the other hand, adopt lower coordination numbers resulting in the sliding of adjacent layer to the (½, 0) configuration (*I*4/*mmm* archetype).[59] All members of the ACI $(GA)(MA)_nPb_nI_{3n+1}$ homology adopt the latter (½, 0) type of the DJ-like perovskite structure albeit in a lower symmetry modification which corresponds to the

"amphoteric" type of oxide DJ perovskites as obtained when 6-coordinated K is used as a spacer and lies between the two archetypes.[29, 59]

The fact that the $(GA)(MA)_nPb_nI_{3n+1}$ compounds adopt the offset layer structure is somewhat surprising given that both GA and MA are significantly larger than Cs.[9] An explanation to this may lie in the fact that the term "coordination" does not strictly apply to the organic cations and trying to compensate for this by means of H-bonding fails since the closest N···I distances are at ~ 3.6 Å for both GA and MA implying only very weak hydrogen bonding.[60] It is perhaps more sensible to assess this effect based on the shape of the two cations which have distinctive triangular (GA) and rod (MA) shapes and due to this "steric hindrance" the perovskite layers offset to accommodate both cations between the two layers in a close-packed arrangement. Note that this DJ-like structural rearrangement observed in the ACI halide perovskites is necessary in order to maintain charge balance, since there is no conceivable charge redistribution between the M^{2+} metal and the A^+ cation to satisfy the genuine DJ structure expressed by the hypothetical "$(GA)(MA)_{n-1}Pb_nI_{3n+1}$" formula. By contrast, transition metal oxide DJ perovskites can maintain charge equilibrium and even interconvert to the RP structure simply by changing the oxidation state of the constituent M^{x+} metal (typically x = 4-5) to compensate for the loss of the A^+ cation.[34] The close-packing of the GA and MA cations can be seen when the arbitrary "coordination" polyhedra around the GA (cutoff distance 4.8 Å) and MA (cutoff distance 4.2 Å) cation are drawn, centered on the carbon atom of each cation, Figure 3. Both cations are 8-coordinate with MA lying in the center of a compressed square prism and GA in the center of an expanded gyrobifastigium. The parallelogram equatorial planes of the two polyhedra reflect clearly the distortion of the perovskite lattice to accommodate the two cations. The equatorial plane of both cations is defined by two parallel vertices that coincide with the crystallographic

axes along the *a*-direction and another two along the *b*-direction. Along *a*-axis the vertices coincide with unit cell parameter (~6.3 Å), whereas along the *b*-axis the vertices deviate with the one around GA expanding to ~7.3 Å whereas the one around MA gets compressed to ~5.2 Å. The geometrical "sum" of these two octahedra has proper dimensions to allow for the doubling of the perovskite layer along the *b*-axis (~12.5 Å) and it is probably responsible for the offset of the adjacent layers.

Because of their specific characteristics, the crystal structures of the ACI perovskites are distinctively different from the corresponding RP perovskites. Using the RP $(BA)_2(MA)_{n-1}Pb_nI_{3n+1}$ series as a reference example,[6] the most distinctive differences can be summarized as follows: i) RP perovskites exhibit a significant distortion in both *a* and *b* crystallographic directions owing to the distortive nature of the bulky BA spacers which exert a strong disruptive force at the perovskite edges. In ACI perovskites, however, the combination of the MA/GA cations which pack tightly between the layers causes the distortion to be minimized in only one direction. Using the crystallographic nomenclature (Glazer[61] in parenthesis or Aleksandrov[53] in square brackets), the individual layers in the BA series is characterized by a $(a^-a^0a^-)$ [$\Phi 0\Phi$] tilting mode whereas the GA/MA series by a $(a^+a^0a^0)$ [$\Psi 00$] mode. Remarkably, none of these two series has any significant distortion along the stacking direction, unlike the corresponding PEA series (PEA is phenylethylammonium)[8, 62] which shows a tilting preference along the stacking axis adopting a $(a^0a^0a^+)$ [00Ψ] tilting mode. ii) As a result of the more tidy packing of the cations, ACI perovskites are more symmetric as reflected in the shape of the unit cell [a x $2a$ x $2(a \cdot n+x)$] which is closer to the α-phase of the 3D perovskite as opposed to the RP perovskites [$\sqrt{a}$ x $\sqrt{a}$ x $2(a \cdot n+x)$]. The latter are better described as a derivative of the β-$MAPbI_3$ phase at room temperature.

Optical Properties. It is very interesting to investigate in the new structure types in 2D halide perovskites how these small structural changes affect the electronic structure of the material *vis-à-vis* the RP phases and consequently their photophysical properties. Figures 4a-c shows the absorption spectra of the $(GA)(MA)_nPb_nI_{3n+1}$ perovskites (n = 1-3). The spectra of all three compounds exhibit a progressive decrease in the bandgap starting from E_g = 2.27 eV for n = 1 to E_g = 1.99 eV for n = 2 and E_g = 1.73 eV for n = 3. The bandgap value is estimated by extrapolating the high-energy edge to the energy axis, since the presence of excitonic peaks in all spectra precludes the observation of a clear band edge. Similar to the RP perovskites, the intensity of the excitonic peaks also decreases with increasing n in ACI perovskites as a consequence of the decrease in the dielectric confinement.[6] However, the absorption edge and the exciton peak position is red shifted in ACI perovskites when compared to the RP perovskites. This is also reflected in the color of the $(GA)(MA)_nPb_nI_{3n+1}$ compounds which changes from red (n = 1) to dark red (n = 2) to black (n = 3), whereas the more established BA-based RP series display a corresponding color change from orange (n = 1) to red (n = 2) to dark red (n = 3), Figures 4a-c.

A plausible, but not conclusive, explanation for this behavior is the symmetry (degree of distortion) in the corresponding perovskites.[63] As mentioned above, the ACI perovskites are distorted only along one dimension (the GA/MA ordering axis), whereas the RP perovskites are distorted along both directions in the *ab*-plane. The higher symmetry of the ACI perovskites is clearly reflected in the corresponding Pb-I-Pb angles which show the tilting along the *a*-axis to be marginal (176-180^o), along the *b*-axis large (~160^o) and intermediate along the stacking *c*-axis (165-167^o). The trend is markedly different from the RP perovskites which see a more uniform deformation with the corresponding Pb-I-Pb angles ranging between 165-170^o for both the *ac*-

plane and the stacking *b*-axis.[6] This symmetry argument, stating that the less distorted crystal structure will have the narrowest bandgap that applies to the 3D halide perovskites,[10] likely applies to the 2D perovskites as well, with the ACI and RP perovskites being the primary examples. In order to better illustrate the bandgap reduction effect, the absorption edges of the n = 1 members of the ACI, RP and <110>-sliced perovskites are plotted in Figure 4d. The observed trend reinforces the symmetry argument since it shows that the most distorted structure of the <110>-sliced perovskite GA_2PbI_4 ($P2_1/n$, E_g = 2.49 eV)[40] has by far the widest bandgap. This is due to the larger distortion and the dihedral angle dependence introduced by the <110> cleavage of the perovskite sheets. [11] This can be compared to to the regular absorption of the less distorted RP perovskite BA_2PbI_4 at E_g = 2.35 eV[6] and the $GAMAPbI_4$ ACI perovskite at E_g = 2.27 eV.

The reason that the symmetry argument discussed above may not hold in full in the 2D perovskites is that other factors such as the contribution of spacer cations to the dielectric confinement or their close proximity of the perovskite layers can be significant. As first pointed out by Ishihara,[64] the dielectric constant of the spacer can dramatically influence the excitons in in 2D perovskites pinpointing the effect of conjugated organic molecules to the binding energy of the confined exciton. The photo-physical puzzle of the 2D materials becomes even more complex if one considers that the precise determination of the band edge continuum relative to the exciton energy level may be challenging,[3, 65] and that the mechanism of the exciton expression also shows a strong temperature dependence.[66] Nevertheless, on first approximation, the excitonic emission as this gets expressed using photoluminescence (PL) spectroscopy does not seem to be affected by these considerations, Figure 5.

The PL spectra of the $(GA)(MA)_nPb_nI_{3n+1}$ ACI perovskite family (Figure 5) follows a similar trend as the absorption spectra, with the PL emission wavelength increasing with

increasing n. The red shift in absorption observed for the ACI perovskites, relative to the RP perovskites, holds firmly in the PL spectra as well. The marked difference between the spectra of the two 2D families is that the ACI perovskites show significantly reduced PL emission intensity relative to the RP series under comparable excitation conditions suggesting that the effect of the dielectric environment due to the conjugated nature of the GA cations or the close proximity between the perovskite layers has a significant effect. Although the present work is not an exhaustive study of the optical properties of the new ACI perovskites, it is already obvious that the properties of all 2D halide perovskites are significantly influenced by subtle structural changes and thus offer a wide field for further investigations.

Band structure. The electronic band structure of the $(GA)(MA)_nPb_nI_{3n+1}$ perovskites (n = 1-3) was determined by means of Density Functional Theory (DFT) calculations. The calculations indicate that both the n = 1 and n = 3 members are direct bandgaps semiconductors at the R point of the Brillouin zone whereas the n = 2 member has a slightly indirect bandgap at the S point, Figure 6a. The n = 2 member shows a slight deviation from the typical direct bandgap behavior, observed in halide perovskites because of strong Rashba splitting caused by the noncentrosymmetric nature of its structure (Figure S1). The calculated bandgaps are underestimated within their typical margins at this level of theory but they nicely agree with the experimental trends for the ACI $(GA)(MA)_nPb_nI_{3n+1}$ perovskites of E_g = 1.12 eV (n = 1), E_g = 0.75 eV (n = 2) and E_g = 0.12 eV (n = 3). Noteworthy, at the same level of calculation, the corresponding bandgaps for the RP $(BA)_2(MA)_{n-1}Pb_nI_{3n+1}$ perovskites amount to E_g = 1.17 eV (n = 1), E_g = 0.74 eV (n = 2) and E_g = 0.49 eV (n = 3) again predicting the experimental trend (with the exception of n=2).

A remarkable feature observed in the ACI perovskites comes from the fact that they show a small but significant dispersion along the perovskite layer stacking direction (Figure 6a and Table S7; along W-T for n = 1 and Y-Γ for n = 2), suggesting that the structures of the ACI perovskites have a weak but noticeable 3D character. The effect is greater at the valence band maximum (VBM) than at conduction band minimum (CBM; Table S7) and is likely due to the short spacing between the layers (~ 3.1 Å) that is comparable with the Pb-I bonding within the perovskite layers (~ 3.2 Å). In fact, the short spacing allows for additional anti-bonding interaction between iodine p-orbitals (Figure 6b), leading to a greater destabilization of the VBM at the edge of the Brillouin zone. Interestingly, the bands stop being dispersive between the layers for n = 3 (< 1meV) resulting in the typical 2D perovskite picture which has nearly flat bands along the layer stacking direction (e.g. < 1meV for the n = 1-3 RP $(BA)_2(MA)_{n-1}Pb_nI_{3n+1}$). However, the reasons for the almost vanishing dispersion are different in the two cases. In the typical 2D RP perovskites the interlayer distance is large leading to a vanishing electronic coupling along the stacking direction. In addition, for the n = 3 ACI perovskite, the VBM becomes localized on the middle perovskite layer with no weight on the iodides pointing towards the spacing layer (Figure 6b). This localization, in turn, leads to the absence of inter-perovskite layer electronic coupling. Interestingly, the CBM for the n = 3 localizes on the two outer perovskite layers. By contrast, in the n = 1 perovskite both VBM and CBM reside on the same unique perovskite layer not allowing the charges to be efficiently separated. The localized density of states for the n = 2 ACI perovskite evidences a distinctive feature related to its noncentrosymmetric *Bmm*2 space group and the VBM and CBM are forced to localize on each individual layer finding themselves in a state of "charge-frustration".

In order to assess the effect of the spacer dielectric constant on the dielectric confinement of the ACI perovskites, we calculated the dielectric constant of the $(GA)(MA)_nPb_nI_{3n+1}$ perovskites (n = 1 and 3) of this study to compare to those of the RP $(BA)_2(MA)_{n-1}Pb_nI_{3n+1}$ perovskites (n = 1 and 3, Figure S2).[67-68] We avoid the inclusion of the n = 2 members because the permanent dipole related to the lack of inversion symmetry mentioned above bias the calculation. The calculated dielectric profiles indicate that the dielectric contrast difference between the inorganic and the spacer layers is significantly reduced for the ACI perovskites by a factor of 2 compared to those obtained for the RP perovskites. Using a previously proposed composite approach,[69] we demonstrate that the higher dielectric constant in the spacer layer in ACI perovskites can be attributed to the leakage of electron density from the perovskite layers due to the shorter interlayer spacing, as the contribution of the more polarizable GA/MA pairs is only marginally larger than that of the $(BA)_2$ bilayers (Figure 2d). The reduction of the dielectric confinement effect is expected to reduce the exciton binding energy. This trend holds universally throughout the two perovskite families in which the dielectric constants of the materials increase progressively to reach the maximum value of the dielectric constants found in the n = ∞ member ($MAPbI_3$).

Thin film fabrication and morphology. For solar cell applications, we focused on the compound with the smallest bandgap, $GAMA_3Pb_3I_{10}$ (n = 3). First, thin films of this compound were prepared from 10:1 DMF:DMSO solutions. The synthesized compounds readily dissolve in such solvents, yielding a clear bright yellow solution. It was found that a typical post-annealing method yields a very rough, dull-colored film with a root-mean-square (rms) roughness of 37 nm, Figure 7a. The pinholes found in this type of film are unfavorable for planar solar cell device architectures, creating undesired contacts between the two electrodes that results in poor device

performance.[70] To improve the film quality, we applied the previously reported solvent-engineering method where anti-solvent, specifically chlorobenzene, is dripped during the spinning of the substrate to expedite the solvent removal process and subsequently promotes faster perovskite crystallization.[71-72] This method enables precise control of the perovskite crystallization rate by changing the delay time before the commencement of the spin-casting process and the anti-solvent dropping.

Here we investigated the optimal crystallization rate for $GAMA_3Pb_3I_{10}$ by varying the delay time between 3 s and 50 s. The obtained films exhibit a desirable compact morphology with nm-scale crystallites, a dramatic improvement from the films without the solvent treatment. We find that 20-30 s delay times yield the smoothest, most compact films. Upon the introduction of anti-solvent drip, the film surface rms roughness decreases markedly down to 10 nm for 10-20 s delay times, beyond which it begins to increase again and eventually reaches 35 nm at 50 s, Figure 7b. The PXRD of these films are shown in Figure 7c. All the films were polycrystalline, consistent with the Bragg diffraction rings in the 2D GIWAXS data (Figure S3). Unlike RP perovskites,[2, 4, 8] the present films from ACI perovskites do not orient vertically, presumably due to the shorter spacing between the perovskite layers provided by GA in comparison to BA cations.

Even though the perovskite slab orientation on the substrate is still suboptimal, we fabricated solar cells with high efficiency. We constructed planar device structures sandwiched between a PEDOT:PSS hole transport layer and a PCBM electron transport layer, Figure 8a, since the desirable vertical growth of the layered perovskites is more favorable on flat substrates for efficient charge transport.[2] The perovskite layer was deposited using the fast-crystallization method with anti-solvent dripping, as described above. Following the trend shown in the AFM

images of the films, Figure 6a, which show the rms roughness of the films steadily decreasing down to ~20s anti-solvent dripping delay time and then increasing again after the 30s delay mark, we fabricated devices at the same dripping delay time intervals to study the effect of film morphology on the device performance. Here the delay time is defined as the time between the commencement of the spin-casting process and the dripping of the anti-solvent while the substrate is spinning. The devices without the solvent treatment were not functional because of the high roughness and protruding features on the rough perovskite film which create shorting pathways. We observed a dramatic change in device parameters depending on when the anti-solvent is dropped. As expected, there is a distinct correlation between the device performance and the perovskite film smoothness and compactness. At very short delay times, low photocurrents and low V_{oc} are observed, which improve upon increasing the anti-solvent delay time, Figure 8.

Remarkably, a significant improvement in the overall performance is observed at 10-20 sec delay due to the formation of the compact, smooth film morphology. In particular, at 20 s delay time, a high Voc of ~1V, high Jsc of 9.84 mA/cm^2, and an impressively high FF of 79.68% are obtained. The high V_{oc} illustrates an excellent interface between the perovskite layer and the charge extraction layers. Intriguingly, while 2D perovskites typically suffer from low FF due to the relatively higher charge recombination rate than their 3D counterparts, here we obtain a superior FF, which we attribute to the high-quality film morphology with full surface coverage and minimal pinholes. These qualities are in good agreement with previous studies on $MAPbI_3$ where GA was used as an additive.[73] The main difference between the devices fabricated from the bulk materials as described here vs. devices made by mixing the constituent salts as described by Marco et al.[73] can be seen from the optical absorption spectra and the PXRD patterns of the

films (Figures S3 and S4). Our data clearly identify the active solar absorber to be the title 2D compound, whereas the additive approach yields $MAPbI_3$ as the active absorber.[73] Our results suggest that the ACI perovskites are very promising in giving a competitive device efficiency even without the benefits of preferred orientation,[2, 4] which is an obvious path towards improving device performance in the future.

The present solar cells also show high reproducibility with an average PCE from 10 devices 6.69 ± 0.47%. For longer anti-solvent delay times, the device performance begins to decrease, as evidenced by large drops in V_{oc} and FF on going from 20 sec to 50 sec (Table 4). This may be caused by the increased surface inhomogeneity and roughness as crystallites begin to aggregate and form nanostructures compromising the compactness of the films. It is, however, interesting that the photocurrent did not change significantly for longer delay times, likely because the intrinsic film crystallinity remains unaltered regardless of the delay time.

To ensure fabrication of high efficiency solar cells, it is essential to optimize the light absorber thickness, since the light harvesting ability and carrier diffusion length must be balanced for optimum solar cell efficiency. Thus, we conducted a systematic study of device efficiency as a function of precursor concentration, which in turn determines the perovskite thickness and find an optimized condition at 30 mg in 110 μL solvent mixture (Figure S3). Compared to BA-based n = 3 cells, the photocurrent generated in this GA-based n = 3 devices is comparatively low, likely due to non-optimally oriented nature of the 2D $GAMA_3Pb_3I_{10}$. Work is in progress to further engineer the vertical orientation of the microstructure to further improve device performance.

CONCLUSIONS

A new family of 2D halide perovskites of the formula $(C(NH_2)_3)(CH_3NH_3)_nPb_nI_{3n+1}$ can be created which contains alternating cations in the interlayer space (ACI), by employing guanidinium cations as spacers. The red crystals of $(C(NH_2)_3)(CH_3NH_3)PbI_4$ (n = 1) have an optical gap of 2.27 eV; dark red crystals of $(C(NH_2)_3)(CH_3NH_3)_2Pb_2I_7$ (n = 2) have a 1.99 eV optical gap, and black crystals of $(C(NH_2)_3)(CH_3NH_3)_3Pb_3I_{10}$ (n = 3) have a bandgap of 1.73 eV. These materials have narrower bandgaps in comparison to typical RP perovskites, exhibiting a clear red shift in their optical gaps by 80, 90 and 230 meV, respectively for the corresponding n = 1-3 members. We attribute the reduced bandgap of the ACI perovskites to their less distorted crystal structure, behaving in an analogous manner to the 3D halide perovskites as the A-cation changes from Cs to FA. Theoretical calculations successfully confirm this trend providing further insights in the dielectric confinement of these QW electronic systems, and suggesting a small exciton binding energy, which is beneficial for charge-transport related applications. Our initial attempts to employ these compounds as photo-absorbers in planar solar cells for the higher member of the ACI perovskites, $GAMA_3Pb_3I_{10}$ with the smallest bandgap within the present series, have yielded solar cell devices with a maximum $\eta = 7.26\%$ power conversion efficiency due to an impressive FF of ~ 80%. The superior optoelectronic properties of the 2D ACI perovskites suggest that this new class of compounds can advance photovoltaic research on 2D halide perovskites, offering the possibility of breaching the 15% efficiency threshold. Previously, we reported that the photo-physics of thin Ruddlesden-Popper perovskites films with n>2 are dominated by lower energy states associated with the local intrinsic electronic structure of the edges of the perovskite layers. These states appear to provide a direct pathway for dissociating excitons into longer-lived free-carriers that significantly enhance optoelectronic

device performance. The question arises as to whether the ACI perovskites also exhibit similar edge states and will be the subject of future investigations.

Supporting Information

Additional DFT plots for $GAMA_2Pb_2I_7$ highlighting the noncentrosymmetric features (Rashba splitting) of the compound, dielectric constant calculations, and PXRD and GIWAXS patterns of $GAMA_2Pb_2I_7$ and $GAMA_3Pb_3I_{10}$ are provided in the Supporting Information. Detailed crystallographic tables and crystallographic data in .cif format can be found as supplementary materials. This material is available free of charge via the Internet at http://pubs.acs.org.

Corresponding Author

*m-kanatzidis@northwestern.edu

Author Contributions

[#]These authors contributed equally to this work.

Notes

The authors declare no competing financial interest.

Acknowledgements

Work on the synthesis and characterization of the materials was supported by the U.S. Department of Energy, Office of Science (Grant No. SC0012541). Work on the solar cells fabrication and evaluation was supported as part of the ANSER Center, an Energy Frontier Research Center funded by the US Department of Energy, Office of Science, Office of Basic Energy Sciences (award no. DE-SC0001059). Work at Los Alamos National Laboratory (LANL) was supported by the Laboratory Directed Research & Development program. This work was performed in part at the Center for Integrated Nanotechnologies, an Office of Science

User Facility operated for the US DOE Office of Science. LANL, an affirmative-action equal opportunity employer, is operated by Los Alamos National Security for the National Nuclear Security Administration of the US DOE under contract DE-AC52-06NA25396. C.K. and B.T. acknowledge high-performance computing resources from Grand Equipment National de Calcul Intensif (CINES/IDRIS, grant 2016-[x2016097682]). DFT calculations were performed at the Institut des Sciences Chimiques de Rennes, which received funding from the European Union's Horizon 2020 Programme for Research and Innovation under grant 687008. This work made use of the SPID (confocal microscopy) and EPIC (scanning electron microscopy) facilities of Northwestern University's NU*ANCE* Center, which has received support from the Soft and Hybrid Nanotechnology Experimental Resource (NSF ECCS-1542205), the Materials Research Science and Engineering Centers (NSF DMR-1121262), the International Institute for Nanotechnology (IIN), the Keck Foundation, and the State of Illinois through the IIN. Use of the Advanced Photon Source at Argonne National Laboratory was supported by the Basic Energy Sciences program of the US DOE Office of Science under contract DE-AC02-06CH11357.

References

(1) Stoumpos, C. C.; Soe, C. M. M.; Tsai, H.; Nie, W.; Blancon, J.-C.; Cao, D. H.; Liu, F.; Traoré, B.; Katan, C.; Even, J.; Mohite, A. D.; Kanatzidis, M. G., High Members of the 2D Ruddlesden-Popper Halide Perovskites: Synthesis, Optical Properties, and Solar Cells of $(CH_3(CH_2)_3NH_3)_2(CH_3NH_3)_4Pb_5I_{16}$. *Chem* **2017,** *2*, 427-440.

(2) Tsai, H.; Nie, W.; Blancon, J.-C.; Stoumpos, C. C.; Asadpour, R.; Harutyunyan, B.; Neukirch, A. J.; Verduzco, R.; Crochet, J. J.; Tretiak, S.; Pedesseau, L.; Even, J.; Alam, M. A.; Gupta, G.; Lou, J.; Ajayan, P. M.; Bedzyk, M. J.; Kanatzidis, M. G.; Mohite, A. D., High-efficiency two-dimensional Ruddlesden–Popper perovskite solar cells. *Nature* **2016,** *536*, 312-316.

(3) Blancon, J.-C.; Tsai, H.; Nie, W.; Stoumpos, C. C.; Pedesseau, L.; Katan, C.; Kepenekian, M.; Soe, C. M. M.; Appavoo, K.; Sfeir, M. Y.; Tretiak, S.; Ajayan, P. M.; Kanatzidis, M. G.; Even, J.; Crochet, J. J.; Mohite, A. D., Extremely efficient internal exciton dissociation through edge states in layered 2D perovskites. *Science* **2017,** *355*, 1288-1292.

(4) Cao, D. H.; Stoumpos, C. C.; Farha, O. K.; Hupp, J. T.; Kanatzidis, M. G., 2D Homologous Perovskites as Light-Absorbing Materials for Solar Cell Applications. *J. Am. Chem. Soc.* **2015,** *137*, 7843-50.

(5) Mao, L.; Tsai, H.; Nie, W.; Ma, L.; Im, J.; Stoumpos, C. C.; Malliakas, C. D.; Hao, F.; Wasielewski, M. R.; Mohite, A. D.; Kanatzidis, M. G., Role of Organic Counterion in Lead- and Tin-based Two-dimensional Semiconducting Iodide Perovskites and Application in Planar Solar Cells. *Chem. Mater.* **2016,** *28*, 7781-7792.

(6) Stoumpos, C. C.; Cao, D. H.; Clark, D. J.; Young, J.; Rondinelli, J. M.; Jang, J. I.; Hupp, J. T.; Kanatzidis, M. G., Ruddlesden–Popper Hybrid Lead Iodide Perovskite 2D Homologous Semiconductors. *Chem. Mater.* **2016,** *28*, 2852-2867.

(7) Mao, L.; Wu, Y.; Stoumpos, C. C.; Wasielewski, M. R.; Kanatzidis, M. G., White-light Emission and Structural Distortion in New Corrugated 2D Lead Bromide Perovskites. *J. Am. Chem. Soc.* **2017,** *139*, 5210–5215.

(8) Smith, I. C.; Hoke, E. T.; Solis-Ibarra, D.; McGehee, M. D.; Karunadasa, H. I., A Layered Hybrid Perovskite Solar-Cell Absorber with Enhanced Moisture Stability. *Angew. Chem. Int. Ed.* **2014,** *53*, 11232-11235.

(9) Kieslich, G.; Sun, S.; Cheetham, A. K., Solid-state principles applied to organic-inorganic perovskites: new tricks for an old dog. *Chem. Sci.* **2014,** *5*, 4712-4715.

(10) Stoumpos, C. C.; Kanatzidis, M. G., The Renaissance of Halide Perovskites and Their Evolution as Emerging Semiconductors. *Acc. Chem. Res.* **2015,** *48*, 2791-802.

(11) Stoumpos, C. C.; Mao, L.; Malliakas, C. D.; Kanatzidis, M. G., Structure–Band Gap Relationships in Hexagonal Polytypes and Low-Dimensional Structures of Hybrid Tin Iodide Perovskites. *Inorg. Chem.* **2017,** *56*, 56-73.

(12) Papavassiliou, G. C.; Koutselas, I. B., Structural, optical and related properties of some natural three- and lower-dimensional semiconductor systems. *Synth. Met.* **1995,** *71*, 1713-1714.

(13) Sourisseau, S.; Louvain, N.; Bi, W.; Mercier, N.; Rondeau, D.; Boucher, F.; Buzaré, J.-Y.; Legein, C., Reduced Band Gap Hybrid Perovskites Resulting from Combined Hydrogen and Halogen Bonding at the Organic−Inorganic Interface. *Chem. Mater.* **2007,** *19*, 600-607.

(14) Billing, D. G.; Lemmerer, A., Inorganic-organic hybrid materials incorporating primary cyclic ammonium cations: The lead iodide series. *CrystEngComm* **2007,** *9*, 236-244.

(15) Mitzi, D. B., Organic−Inorganic Perovskites Containing Trivalent Metal Halide Layers: The Templating Influence of the Organic Cation Layer. *Inorg. Chem.* **2000,** *39*, 6107-6113.

(16) Wang, S.; Mitzi, D. B.; Feild, C. A.; Guloy, A., Synthesis and Characterization of $[NH_2C(I):NH_2]_3MI_5$ (M = Sn, Pb): Stereochemical Activity in Divalent Tin and Lead Halides Containing Single <110> Perovskite Sheets. *J. Am. Chem. Soc.* **1995,** *117*, 5297-5302.
(17) A. Mousdis, G.; Gionis, V.; C. Papavassiliou, G.; P. Raptopoulou, C.; Terzis, A., Preparation, structure and optical properties of $[CH_3SC(NH_2)_2]_3PbI_5$, $[CH_3SC(NH_2)_2]_4Pb_2Br_8$ and $[CH_3SC(NH_2)_2]_3PbCl_5{\cdot}CH_3SC(NH_2)_2Cl$. *J. Mater. Chem.* **1998,** *8*, 2259-2262.
(18) Zimmermann, I.; Keene, T. D.; Hauser, J.; Decurtins, S.; Liu, S.-X., Crystal structures of isotypic poly[bis(benzimidazolium) [tetra-[mu]-iodido-stannate(II)]] and poly[bis(5,6-difluorobenzimidazolium) [tetra-[mu]-iodido-stannate(II)]]. *Acta Crystallogr. E* **2014,** *70*, 178-182.
(19) Apostolico, L.; Kociok-Kohn, G.; Molloy, K. C.; Blackman, C. S.; Carmalt, C. J.; Parkin, I. P., The reaction of tin(iv) iodide with phosphines: formation of new halotin anions. *Dalton Trans.* **2009**, 10486-10494.
(20) Ruddlesden, S. N.; Popper, P., The compound $Sr_3Ti_2O_7$ and its structure. *Acta Crystallogr.* **1958,** *11*, 54-55.
(21) Ruddlesden, S. N.; Popper, P., New compounds of the K_2NiF_4 type. *Acta Crystallogr.* **1957,** *10*, 538-539.
(22) Dion, M.; Ganne, M.; Tournoux, M., Nouvelles familles de phases $M(I)M(II)_2Nb_3O_{10}$ a feuillets "perovskites". *Mater. Res. Bull.* **1981,** *16*, 1429-1435.
(23) Jacobson, A. J.; Johnson, J. W.; Lewandowski, J. T., Interlayer chemistry between thick transition-metal oxide layers: synthesis and intercalation reactions of $K[Ca_2Na_{n-3}Nb_nO_{3n+1}]$ ($3 \leq n \leq 7$). *Inorg. Chem.* **1985,** *24*, 3727-3729.
(24) Aurivillius, B., Mixed bismuth oxides with layer lattices. The structure type of $CaNb_2Bi_2O_9$. *Arkiv for Kemi* **1949,** *1*, 463-480.
(25) Aurivillius, B., Mixed bismuth oxides with layer lattices. Structure of $Bi_4Ti_3O_{12}$. *Arkiv for Kemi* **1949,** *1*, 499-512.
(26) Aurivillius, B., Mixed bismuth oxides with layer lattices. Structure of $BaBi_4Ti_4O_{15}$. *Arkiv for Kemi* **1950,** *2*, 519-527.
(27) Hervoches, C. H.; Lightfoot, P., A Variable-Temperature Powder Neutron Diffraction Study of Ferroelectric Bi4Ti3O12. *Chem. Mater.* **1999,** *11*, 3359-3364.
(28) Kendall, K. R.; Navas, C.; Thomas, J. K.; zur Loye, H.-C., Recent Developments in Oxide Ion Conductors: Aurivillius Phases. *Chem. Mater.* **1996,** *8*, 642-649.
(29) Sato, M.; Abo, J.; Jin, T.; Ohta, M., Structure determination of $KLaNb_2O_7$ exhibiting ion exchange ability by X-ray powder diffraction. *Solid State Ion.* **1992,** *51*, 85-89.
(30) Kumada, N.; Kinomura, N.; Sleight, A. W., $CsLaNb_2O_7$. *Acta Crystallogr. C* **1996,** *52*, 1063-1065.
(31) Strayer, M. E.; Gupta, A. S.; Akamatsu, H.; Lei, S.; Benedek, N. A.; Gopalan, V.; Mallouk, T. E., Emergent Noncentrosymmetry and Piezoelectricity Driven by Oxygen Octahedral Rotations in n = 2 Dion–Jacobson Phase Layer Perovskites. *Adv. Funct. Mater.* **2016,** *26*, 1930-1937.
(32) Benedek, N. A.; Rondinelli, J. M.; Djani, H.; Ghosez, P.; Lightfoot, P., Understanding ferroelectricity in layered perovskites: new ideas and insights from theory and experiments. *Dalton Trans.* **2015,** *44*, 10543-10558.
(33) Benedek, N. A., Origin of Ferroelectricity in a Family of Polar Oxides: The Dion—Jacobson Phases. *Inorg. Chem.* **2014,** *53*, 3769-3777.

(34) Schaak, R. E.; Mallouk, T. E., Perovskites by Design: A Toolbox of Solid-State Reactions. *Chem. Mater.* **2002,** *14*, 1455-1471.
(35) Stoumpos, C. C.; Malliakas, C. D.; Kanatzidis, M. G., Semiconducting Tin and Lead Iodide Perovskites with Organic Cations: Phase Transitions, High Mobilities, and Near-Infrared Photoluminescent Properties. *Inorg. Chem.* **2013,** *52*, 9019-9038.
(36) Mitzi, D. B.; Wang, S.; Feild, C. A.; Chess, C. A.; Guloy, A. M., Conducting Layered Organic-inorganic Halides Containing -Oriented Perovskite Sheets. *Science* **1995,** *267*, 1473-1476.
(37) Grottel, M.; Szafrański, M.; Pająk, Z., NMR Study of Cation Motion in Guanidinium Iodoplumbates. *Z. Naturforsch. A* **1997,** *52*, 783.
(38) Szafrański, M.; Katrusiak, A., Phase transitions in the layered structure of diguanidinium tetraiodoplumbate. *Phys. Rev. B* **2000,** *61*, 1026-1035.
(39) Szafrański, M.; Ståhl, K., Pressure-induced decoupling of the order-disorder and displacive contributions to the phase transition in diguanidinium tetrachlorostannate. *Phys. Rev. B* **2000,** *62*, 8787-8793.
(40) Daub, M.; Haber, C.; Hillebrecht, H., Synthesis, Crystal Structures, Optical Properties, and Phase Transitions of the Layered Guanidinium-Based Hybrid Perovskites $[C(NH_2)_3]_2MI_4$; M = Sn, Pb. *Eur. J. Inorg. Chem.* **2017,** *2017*, 1120-1126.
(41) Nazarenko, O.; Kotyrba, M. R.; Wörle, M.; Cuervo-Reyes, E.; Yakunin, S.; Kovalenko, M. V., Luminescent and Photoconductive Layered Lead Halide Perovskite Compounds Comprising Mixtures of Cesium and Guanidinium Cations. *Inorg. Chem.* **2017,** *56*, 11552-11564.
(42) Gate, L. F., Comparison of the Photon Diffusion Model and Kubelka-Munk Equation with the Exact Solution of the Radiative Transport Equation. *Appl. Opt.* **1974,** *13*, 236-238.
(43) Chondroudis, K.; McCarthy, T. J.; Kanatzidis, M. G., Chemistry in Molten Alkali Metal Polyselenophosphate Fluxes. Influence of Flux Composition on Dimensionality. Layers and Chains in APbPSe4, A4Pb(PSe4)2 (A = Rb, Cs), and K4Eu(PSe4)2. *Inorg. Chem.* **1996,** *35*, 840-844.
(44) McCarthy, T. J.; Kanatzidis, M. G., Synthesis in Molten Alkali Metal Polyselenophosphate Fluxes: A New Family of Transition Metal Selenophosphate Compounds, $A_2MP_2Se_6$ (A = K, Rb, Cs; M = Mn, Fe) and $A_2M'_2P_2Se_6$ (A = K, Cs; M' = Cu, Ag). *Inorg. Chem.* **1995,** *34*, 1257-1267.
(45) Petříček, V.; Dušek, M.; Palatinus, L., Crystallographic Computing System JANA2006: General features. *Z. Kristallogr* **2014,** *229*, 345.
(46) Spek, A., Structure validation in chemical crystallography. *Acta Crystallogr. D* **2009,** *65*, 148-155.
(47) José, M. S.; Emilio, A.; Julian, D. G.; Alberto, G.; Javier, J.; Pablo, O.; Daniel, S.-P., The SIESTA method for ab initio order- N materials simulation. *J. Phys.: Cond. Matter* **2002,** *14*, 2745.
(48) Perdew, J. P.; Burke, K.; Ernzerhof, M., Generalized Gradient Approximation Made Simple. *Phys. Rev. Lett.* **1996,** *77*, 3865-3868.
(49) Fernández-Seivane, L.; Oliveira, M. A.; Sanvito, S.; Ferrer, J., On-site approximation for spin–orbit coupling in linear combination of atomic orbitals density functional methods. *J. Phys.: Cond. Matter* **2006,** *18*, 7999.
(50) Troullier, N.; Martins, J. L., Efficient pseudopotentials for plane-wave calculations. *Phys. Rev. B* **1991,** *43*, 1993-2006.

(51) Artacho, E.; Sánchez-Portal, D.; Ordejón, P.; García, A.; Soler, J. M., Linear-Scaling ab-initio Calculations for Large and Complex Systems. *Phys. Status Sol. B* **1999,** *215*, 809-817.
(52) Mitzi, D. B.; Liang, K.; Wang, S., Synthesis and Characterization of $[NH_2C(I)NH_2]_2ASnI_5$ with A = Iodoformamidinium or Formamidinium: The Chemistry of Cyanamide and Tin(II) Iodide in Concentrated Aqueous Hydriodic Acid Solutions. *Inorg. Chem.* **1998,** *37*, 321-327.
(53) Aleksandrov, K. S., Structural Phase Transitions in Layered Perovskitelike Crystals. *Crystallogr. Rep.* **1995,** *40*, 279-301.
(54) Mercier, N., $(HO_2C(CH_2)_3NH_3)_2(CH_3NH_3)Pb_2I_7$: a predicted non-centrosymmetrical structure built up from carboxylic acid supramolecular synthons and bilayer perovskite sheets. *CrystEngComm* **2005,** *7*, 429-432.
(55) Szafrański, M.; Katrusiak, A., Mechanism of Pressure-Induced Phase Transitions, Amorphization, and Absorption-Edge Shift in Photovoltaic Methylammonium Lead Iodide. *J. Phys. Chem. Lett.* **2016,** *7*, 3458-3466.
(56) Hamilton, W., Significance tests on the crystallographic R factor. *Acta Crystallogr.* **1965,** *18*, 502-510.
(57) Rogers, D., On the application of Hamilton's ratio test to the assignment of absolute configuration and an alternative test. *Acta Crystallogr. A* **1981,** *37*, 734-741.
(58) The discussion and notation are quoted from: https://www.princeton.edu/~cavalab/tutorials/public/structures/perovskites.html. Accessed on 06/2017.
(59) Fukuoka, H.; Isami, T.; Yamanaka, S., Crystal Structure of a Layered Perovskite Niobate $KCa_2Nb_3O_{10}$. *J. Solid State Chem.* **2000,** *151*, 40-45.
(60) Steiner, T., The Hydrogen Bond in the Solid State. *Angew. Chem., Int. Ed.* **2002,** *41*, 48-76.
(61) Glazer, A., The classification of tilted octahedra in perovskites. *Acta Crystallographica Section B* **1972,** *28*, 3384-3392.
(62) Calabrese, J.; Jones, N. L.; Harlow, R. L.; Herron, N.; Thorn, D. L.; Wang, Y., Preparation and characterization of layered lead halide compounds. *J. Am. Chem. Soc.* **1991,** *113*, 2328-2330.
(63) Pedesseau, L.; Sapori, D.; Traore, B.; Robles, R.; Fang, H.-H.; Loi, M. A.; Tsai, H.; Nie, W.; Blancon, J.-C.; Neukirch, A.; Tretiak, S.; Mohite, A. D.; Katan, C.; Even, J.; Kepenekian, M., Advances and Promises of Layered Halide Hybrid Perovskite Semiconductors. *ACS Nano* **2016,** *10*, 9776-9786.
(64) Hong, X.; Ishihara, T.; Nurmikko, A. V., Dielectric confinement effect on excitons in PbI_4-based layered semiconductors. *Phys. Rev. B* **1992,** *45*, 6961-6964.
(65) Ishihara, T.; Takahashi, J.; Goto, T., Optical properties due to electronic transitions in two-dimensional semiconductors $(C_nH_{2n+1}NH_3)_2PbI_4$. *Phys. Rev. B* **1990,** *42*, 11099-11107.
(66) Yaffe, O.; Chernikov, A.; Norman, Z. M.; Zhong, Y.; Velauthapillai, A.; van der Zande, A.; Owen, J. S.; Heinz, T. F., Excitons in ultrathin organic-inorganic perovskite crystals. *Phys. Rev. B* **2015,** *92*, 045414.
(67) Sapori, D.; Kepenekian, M.; Pedesseau, L.; Katan, C.; Even, J., Quantum confinement and dielectric profiles of colloidal nanoplatelets of halide inorganic and hybrid organic-inorganic perovskites. *Nanoscale* **2016,** *8*, 6369-6378.

(68) Even, J.; Pedesseau, L.; Kepenekian, M., Electronic surface states and dielectric self-energy profiles in colloidal nanoscale platelets of CdSe. *Phys. Chem. Chem. Phys.* **2014,** *16*, 25182-25190.
(69) Even, J.; Pedesseau, L.; Katan, C., Understanding Quantum Confinement of Charge Carriers in Layered 2D Hybrid Perovskites. *ChemPhysChem* **2014,** *15*, 3733-3741.
(70) Soe, C. M. M.; Stoumpos, C. C.; Harutyunyan, B.; Manley, E. F.; Chen, L. X.; Bedzyk, M. J.; Marks, T. J.; Kanatzidis, M. G., Room Temperature Phase Transition in Methylammonium Lead Iodide Perovskite Thin Films Induced by Hydrohalic Acid Additives. *ChemSusChem* **2016,** *9*, 2656-2665.
(71) Jeon, N. J.; Noh, J. H.; Kim, Y. C.; Yang, W. S.; Ryu, S.; Seok, S. I., Solvent engineering for high-performance inorganic–organic hybrid perovskite solar cells. *Nat. Mater.* **2014,** *13*, 897-903.
(72) Xiao, M.; Huang, F.; Huang, W.; Dkhissi, Y.; Zhu, Y.; Etheridge, J.; Gray-Weale, A.; Bach, U.; Cheng, Y.-B.; Spiccia, L., A Fast Deposition-Crystallization Procedure for Highly Efficient Lead Iodide Perovskite Thin-Film Solar Cells. *Angewandte Chemie* **2014,** *126*, 10056-10061.
(73) Marco, N. D.; Zhou, H.; Chen, Q.; Sun, P.; Liu, Z.; Meng, L.; Yao, E.-P.; Liu, Y.; Schiffer, A.; Yang, Y., Guanidinium: A Route to Enhanced Carrier Lifetime and Open-Circuit Voltage in Hybrid Perovskite Solar Cells. *Nano Lett.* **2016,** *16*, 1009-1016.
(74) Shimakawa, Y.; Kubo, Y.; Nakagawa, Y.; Goto, S.; Kamiyama, T.; Asano, H.; Izumi, F., Crystal structure and ferroelectric properties of $ABi_2Ta_2O_9$ (A=Ca, Sr, and Ba). *Phys. Rev. B* **2000,** *61*, 6559-6564.

Figure Captions

Figure 1. (a) Representative SEM images of $(GA)(MA)_nPb_nI_{3n+1}$ (n = 1-3) crystals showing a plate-like crystal morphology. The plates are irregular parallelepipeds growing preferentially along one dimension. The scale bars represent a 50μm length. (b) High resolution synchrotron X-ray data (11-BM, APS, λ = 0.517040 Å) for $(GA)(MA)_nPb_nI_{3n+1}$ (n = 1-3). The experimental data are in excellent agreement with the theoretical patterns determined by single-crystal X-ray diffraction analysis. The impurity observed in the n = 1 perovskite that grows on the surface of the crystal was identified to arise from the n = 2 member and amounts to ~10% of the sample.

Figure 2. View of the unit cells of the $(GA)(MA)_nPb_nI_{3n+1}$ (n = 1-3) perovskites along (a) the crystallographic *b*- and along (b) the crystallographic *a*-axis highlighting the ordered crystal packing of the GA and MA cations between the perovskite layers

Figure 3. (a) Projected view of a supercell of $(GA)(MA)_3Pb_3I_{10}$ along the crystallographic *a*-axis emphasizing on the polyhedral voids between the perovskite layers. (b-c) The "coordination" polyhedra of the GA and MA cations. (b) GA resides in the barycenter of a gyrobifastigium and (c) MA resides in the center of a square prism cavity. (d-f) The crystal packing of the respective polyhedra. (d) Packing of the GA cations along the *a*-axis. (e) Packing of GA and MA along the *b*-axis. (f) Side view of the packing of MA cations along the a-axis.

Figure 4. (a-c) Optical absorption spectra of the $(GA)(MA)_nPb_nI_{3n+1}$ (n = 1-3) perovskites. (d) Selected absorption spectra of n = 1 member of the ACI perovskite $(GA)(MA)PbI_4$, the RP perovskite $(BA)_2PbI_4$ and the (110)-cleaved perovskite $(GA)_2PbI_4$ highlighting the importance of the perovskite structure-type on the optical properties of the materials.

Figure 5. (a-c) Steady-state PL spectra and (d) graphical representation of the $(GA)(MA)_nPb_nI_{3n+1}$ (n = 1-3) ACI perovskites (solid lines) and their comparison with the corresponding n-members of the $(BA)_2(MA)_{n-1}Pb_nI_{3n+1}$ series of RP perovskites.

Figure 6. Electronic structure of the $(GA)(MA)_nPb_nI_{3n+1}$ (n = 1-3) perovskites. (a) Electronic band structure of the n = 1-3 members highlighting the progressive narrowing of the bandgap and the splitting of the band extrema as the number of 2D layers increases. (b) The localized density of states around the conduction band minimum (CBM) and the valence band maximum (VBM), illustrating the propensity of the terminal 2D layers to host the CBM and the central 2D layers to stabilize the VBM.

Figure 7. (a) AFM images of solution-processed thin films of $(GA)(MA)_3Pb_3I_{10}$ as a function of delay time for anti-solvent chlorobenzene (CB) dripping. The scale bar is 2 μm. (b) change in

surface roughness with increasing CB drip delay time. The size of the AFM image is 10 μm x 10 μm, and (c) PXRD of the associated films, illustrating little influence of the anti-solvent delay time on the film crystallinity and orientation.

Figure 8. (a) Planar heterojunction solar cell structure employing $(GA)(MA)_3Pb_3I_{10}$ as a light absorber. (b) J-V curves of $(GA)(MA)_3Pb_3I_{10}$ as a function of delay time for anti-solvent chlorobenzene (CB) dripping, and (c) the corresponding plots J_{sc}, V_{oc}, FF and power conversion efficiency as a function of delay time for anti-solvent dripping.

Figures

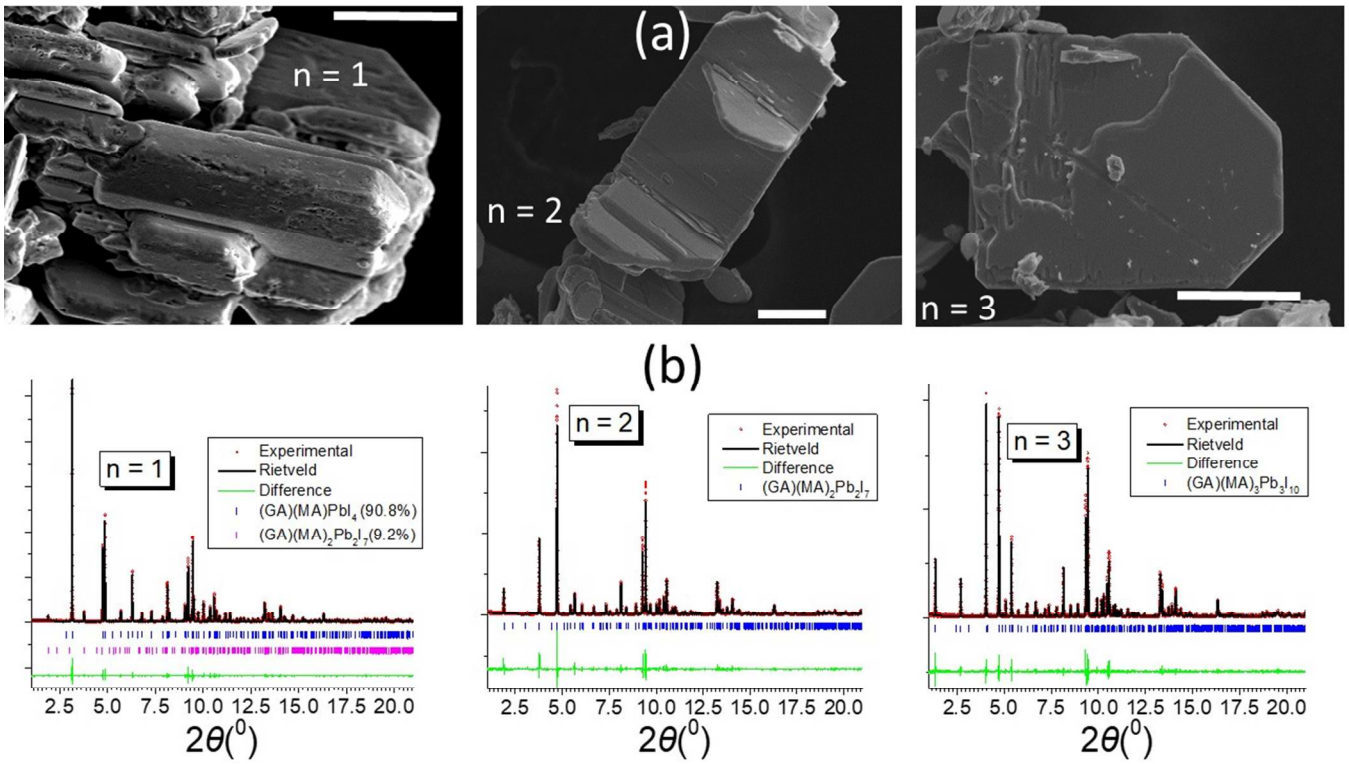

Figure 1

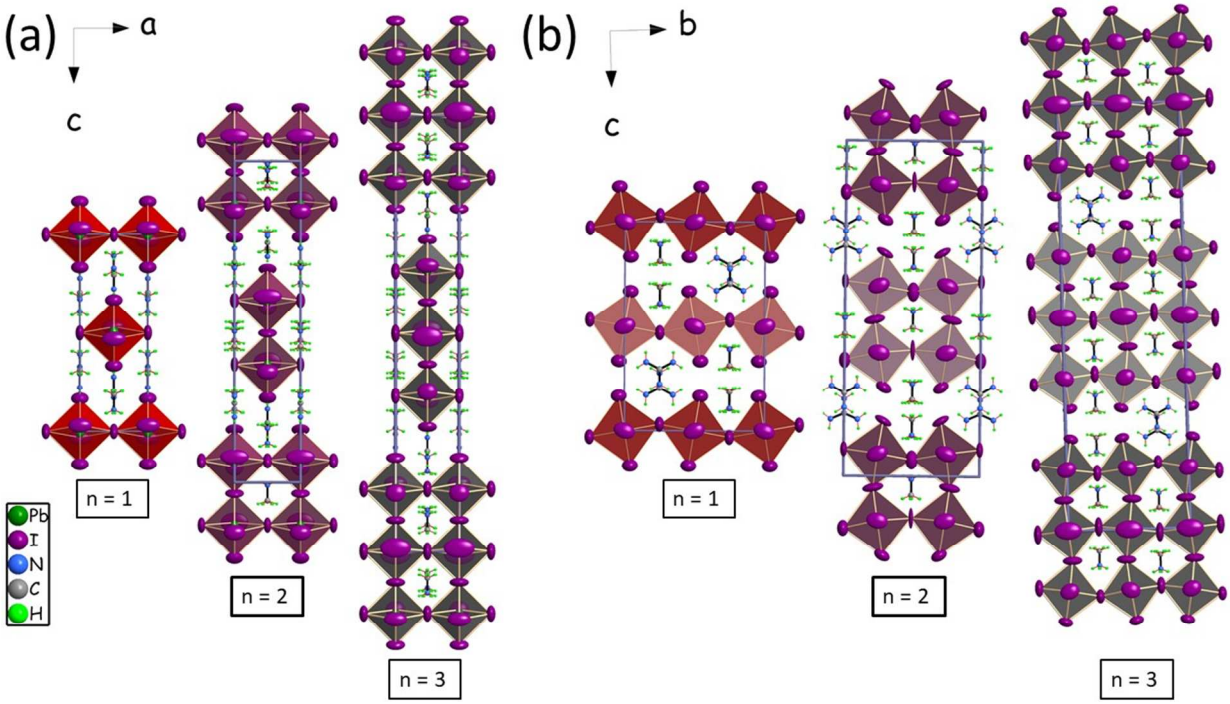

Figure 2

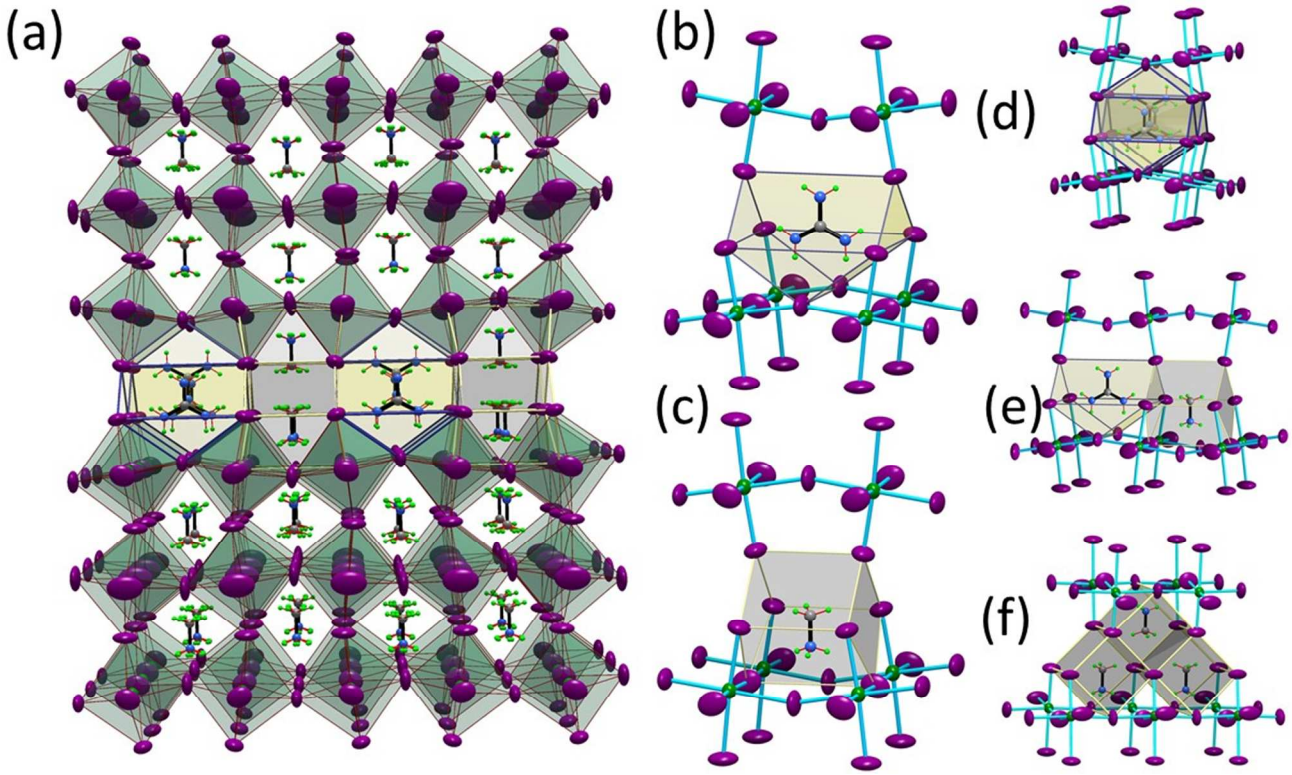

Figure 3

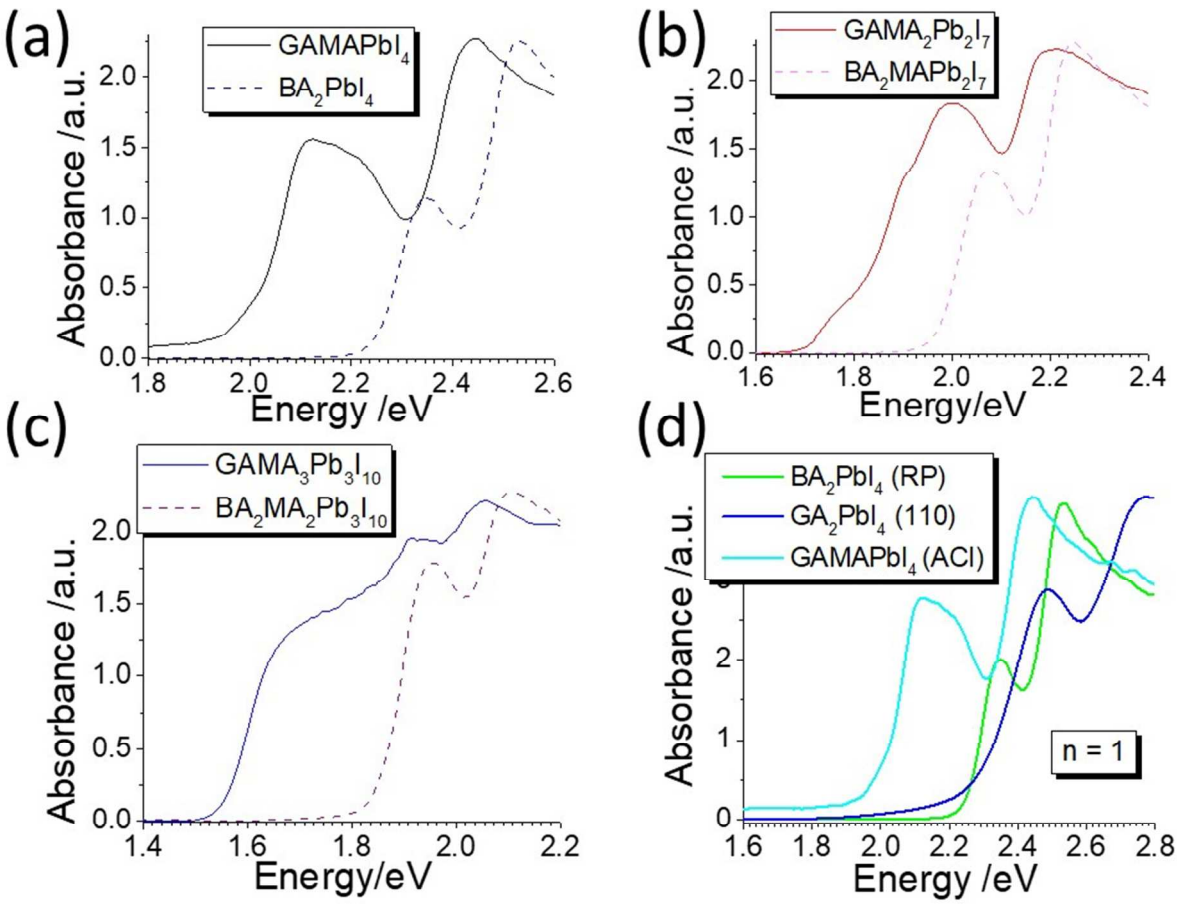
(a)
GAMAPbI4
BA2PbI4
Absorbance /a.u.
Energy /eV
(b)
GAMA2Pb2I7
BA2MAPb2I7
Absorbance /a.u.
Energy/eV
(c)
GAMA3Pb3I10
BA2MA2Pb3I10
Absorbance /a.u.
Energy/eV
(d)
BA2PbI4 (RP)
GA2PbI4 (110)
GAMAPbI4 (ACl)
n = 1
Absorbance /a.u.
Energy /eV

Figure 4

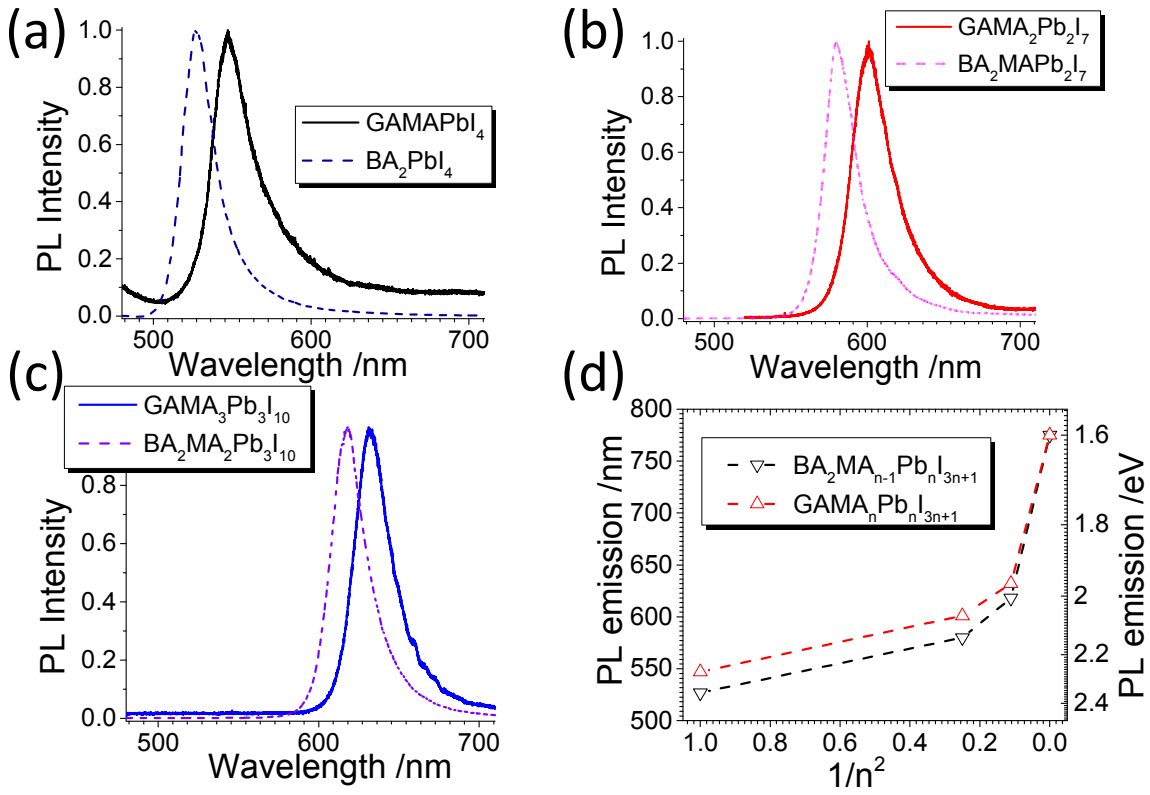
(a)
PL Intensity
Wavelength /nm
GAMAPbI4
BA2PbI4
(b)
PL Intensity
Wavelength /nm
GAMA2Pb2I7
BA2MAPb2I7
(c)
PL Intensity
Wavelength /nm
GAMA3Pb3I10
BA2MA2Pb3I10
(d)
PL emission /nm
PL emission /eV
1/n2
BA2MAn-1PbnI3n+1
GAMAnPbnI3n+1

Figure 5

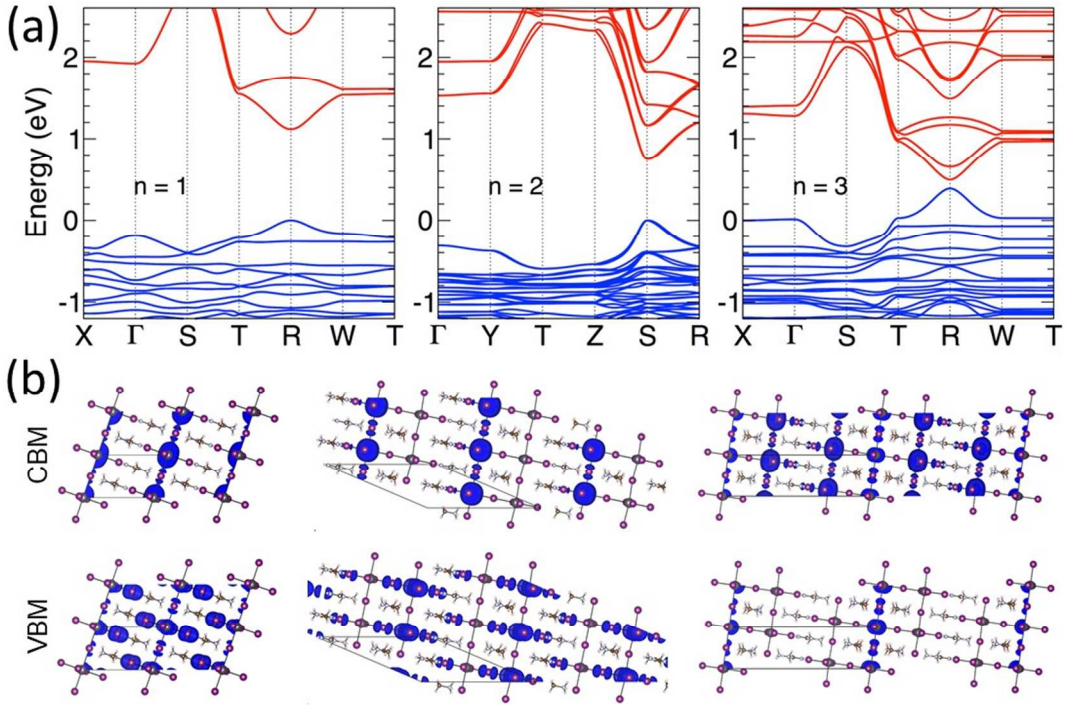

Figure 6

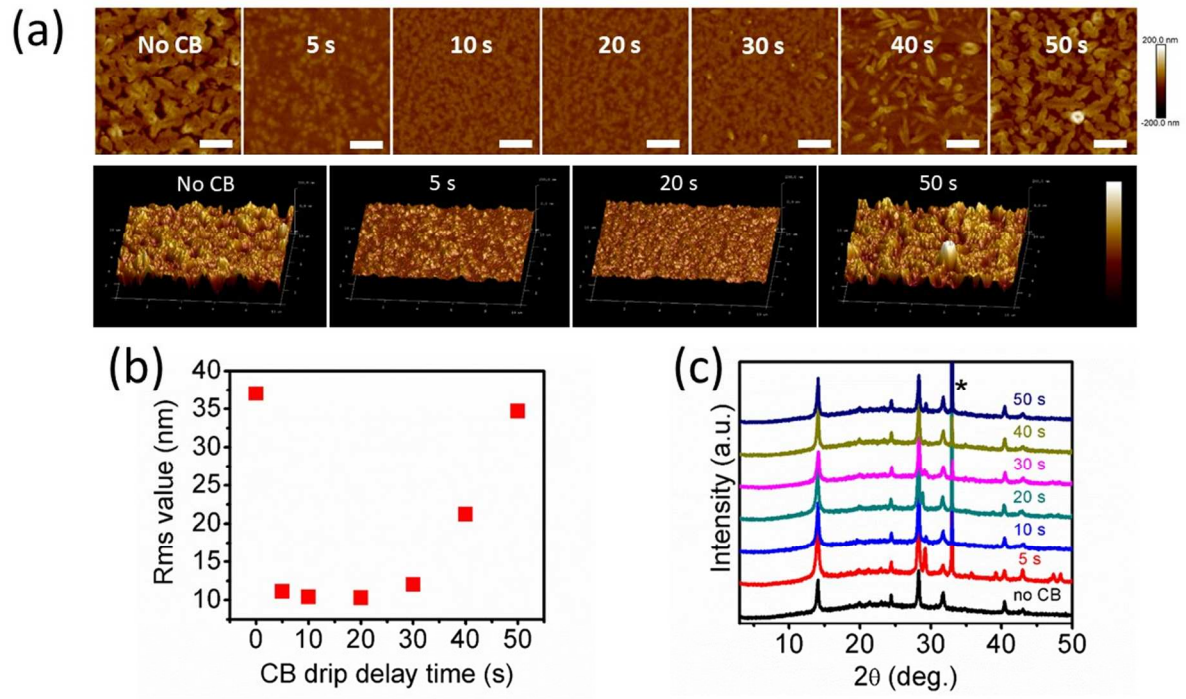
(a)
No CB
5 s
10 s
20 s
30 s
40 s
50 s
200.0 nm
-200.0 nm
No CB
5 s
20 s
50 s
(b)
Rms value (nm)
CB drip delay time (s)
(c)
Intensity (a.u.)
2θ (deg.)
50 s
40 s
30 s
20 s
10 s
5 s
no CB
*

Figure 7

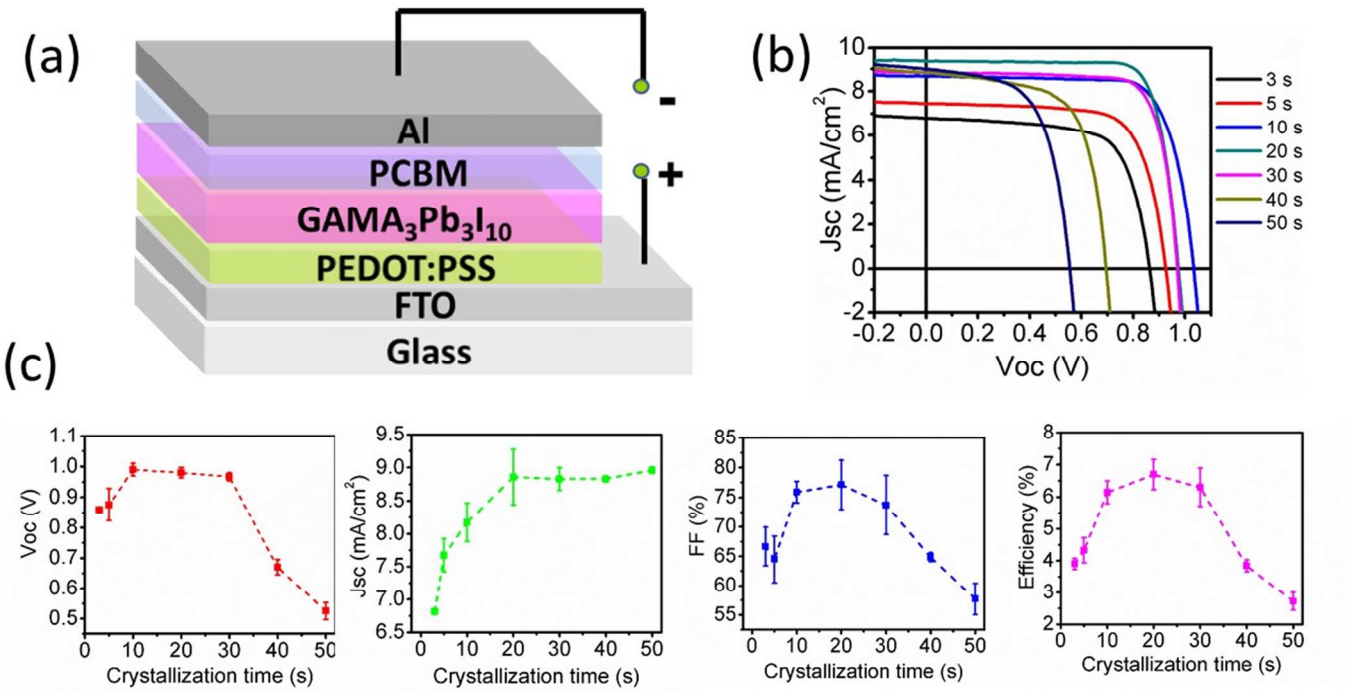
(a)
Al
PCBM
GAMA3Pb3I10
PEDOT:PSS
FTO
Glass
-
+
(b)
Jsc (mA/cm2)
Voc (V)
3 s
5 s
10 s
20 s
30 s
40 s
50 s
(c)
Voc (V)
Jsc (mA/cm2)
FF (%)
Efficiency (%)
Crystallization time (s)

Figure 8

Table 1. Structural configurations of the three types of <100> 2D perovskites.

	RP	DJ	AV	ACI
Formula	$(A'A)_{n+1}B_nX_{3n+1}$	$A'A_{n-1}B_nX_{3n+1}$	$(Bi_2O_2)A_{n-1}B_nX_{3n+1}$	$(A'A)_{n+1}B_nX_{3n+1}$
Stacking sequence	$[(A'X)(ABX)_n]$	$[(A')(A_{n-1}BX)_n]$	$[(Bi_2O_2)(A_{n-1}BX)_n]$	$[(A'X)(ABX)_n]$
Centering of perovskite slabs[a]	*I* (½, ½, ½)	*P* (0,0,0)	*I* (½, ½, ½)	*A/B/C* (½, 0, ½)
n = 3 exemplar	$Sr_4Ti_3O_{10}$	$KCa_2Nb_3O_{10}$	$(Bi_2O_2)SrTa_2O_9$[b,c]	$(GA)(MA)_3Pb_3I_{10}$

[a] in the aristotype, *ie*. ignoring octahedral tilts

[b] The n = 2 is chosen for clarity; for the n = 3 member see reference [27]

[c] Reference [74]

Table 2. Crystal data and structure refinement for $GAMA_nPb_nI_{3n+1}$ (n = 1-3) at 293 K.

Formula	$GAMAPbI_4$	$GAMA_2Pb_2I_7$	$GAMA_3Pb_3I_{10}$
FW	807.0	1426.9	2046.9
Temperature (K)		293	
Wavelength		0.71073 Å	
Refinement method		Full-matrix least-squares on F^2	
Crystal system		orthorhombic	
Space group	*Imma*	*Bmm*2	*Imma*
Unit cell dimensions (Å)	a = 6.4286(6) b = 12.4577(9) c = 18.8258(13)	a = 6.3729(4) b = 12.5435(8) c = 31.376(2)	a = 6.3520(7) b = 12.4378(9) c = 43.970(3)
Volume ($Å^3$)	1507.7(2)	2508.2(3)	3473.8(5)
Z	4	4	4
ρ_{calc} (g/cm^3)	3.5551	3.7788	3.9138
μ (mm^{-1})	19.349	22.017	23.395
F(000)	1392	2424	3464
Crystal size (mm^3)	0.1111 x 0.0225 x 0.0167	0.0511 x 0.179 x 0.0100	0.0733 x 0.0372 x 0.0193
θ range (°)	3.27 to 29.23	2.6 to 29.27	2.78 to 29.29
Index ranges	-8<=h<=8 -17<=k<=16 -25<=l<=25	-8<=h<=8 -17<=k<=17 -42<=l<=42	-8<=h<=8 -17<=k<=16 -57<=l<=60
Reflections collected	7172	11855	12119
Independent reflections	784 [R_{int} = 0.1277]	2595 [R_{int} = 0.0563]	1810 [R_{int} = 0.1261]
Completeness to θ	99%	99%	99%
Data / restraints / parameters	784 / 3 / 28	2595 / 9 / 82	1810 / 5 / 59
GOF	3.18	2.19	2.80
R indices [I>2σ(I)]	R_{obs} = 0.0575 wR_{obs} = 0.1356	R_{obs} = 0.0555 wR_{obs} = 0.1099	R_{obs} = 0.0597 wR_{obs} = 0.1254
R indices [all data]	R_{all} = 0.0677 wR_{all} = 0.1361	R_{all} = 0.0898 wR_{all} = 0.1126	R_{all} = 0.0863 wR_{all} = 0.1270
Largest diff. peak and hole ($e \cdot Å^{-3}$)	1.84 and -2.31	5.69 and -1.65	3.32 and -3.20

$R = \Sigma||F_o|-|F_c|| / \Sigma|F_o|$, $wR = \{\Sigma[w(|F_o|^2 - |F_c|^2)^2] / \Sigma[w(|F_o|^4)]\}^{1/2}$ and $w=1/(\sigma^2(I)+0.0004I^2)$

Table 3. Bond lengths [Å] and angles (degrees) for $GAMAPbI_4$, $GAMA_2Pb_2I_7$, and $GAMA_3Pb_3I_{10}$ at 293 K with estimated standard deviations in parentheses.

$GAMAPbI_4$			
Label	Distances	Label	Angles
Pb(1)-I(1)	3.181(2)	Pb(1)-I(2)-Pb(1)'	180.0(5)
Pb(1)-I(2)	3.2143(6)	Pb(1) -I(3)-Pb(1)'	159.04(13)
Pb(1)-I(3)	3.1673(8)		
$GAMA_2Pb_2I_7$			
Label	Distances	Label	Angles
Pb(1)-I(1)	3.168(3)	Pb(1)-I(1)-Pb(1)'	159.8(4)
Pb(1)-I(4)	3.271(9)	Pb(2)-I(2)-Pb(2)'	159.4(5)
Pb(1)-I(5)	3.121(7)	Pb(1)-I(4)-Pb(2)	166.13(14)
Pb(1)-I(6)	3.1910(6)	Pb(1)-I(6)-Pb(1)'	173.9(3)
Pb(1)-I(8)	3.181(3)	Pb(1)-I(8)-Pb(1)'	164.9(5)
Pb(2)-I(2)	3.205(4)	Pb(2)-I(9)-Pb(2)'	165.1(4)
Pb(2)-I(3)	3.097(7)		
Pb(2)-I(4)	3.206(9)		
Pb(2)-I(7)	3.1865(4)		
Pb(2)-I(9)	3.145(3)		
$GAMA_3Pb_3I_{10}$			
Label	Distances	Label	Angles
Pb(1)-I(5)	3.154(3)	Pb(2)-I(4)-Pb(2)'	162.70(14)
Pb(1)-I(6)	3.1760(7)	Pb(1)-I(5)-Pb(2)	167.66(11)
Pb(1)-I(7)	3.1280(7)	Pb(1)-I(6)-Pb(1)'	180.0(5)
Pb(2)-I(1)	3.092(2)	Pb(1) -I(7)-Pb(1)'	167.50(19)
Pb(2)-I(2)	3.1663(13)		
Pb(2)-I(3)	3.1779(7)		
Pb(2)-I(4)	3.1294(13)		
Pb(2)-I(5)	3.264(3)		

Table 4. Solar cell device parameters for $GAMA_3Pb_3I_{10}$ as a function of the delay in the anti-solvent dripping. The average PCE is obtained from at least ten devices at each condition.

Delay time (s)	Jsc [mA/cm^2]	Voc [V]	FF [%]	η[%]
3 s	6.781	0.863	69.07	4.04 (3.90 ± 0.18)
5 s	7.446	0.925	71.86	4.95 (4.33 ± 0.40)
10 s	8.668	1.033	76.08	6.81 (6.14 ± 0.36)
20 s	9.357	0.974	79.68	7.26 (6.69 ± 0.47)
30 s	8.833	0.970	78.01	6.68 (6.30 ± 0.59)
40 s	8.821	0.695	65.44	4.01 (3.84 ± 0.19)
50 s	8.989	0.554	60.83	3.03 (2.72 ± 0.28)

TOC Image

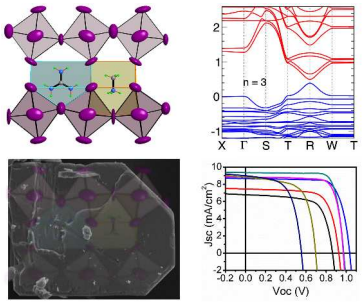

Supporting Information

New Type of 2D Perovskites with Alternating Cations in the Interlayer Space, $(C(NH_2)_3)(CH_3NH_3)_nPb_nI_{3n+1}$: Structure, Properties and Photovoltaic Performance

Chan Myae Myae Soe,[1#] Constantinos C. Stoumpos,[1#] Mikaël Kepenekian,[2] Boubacar Traoré,[2] Hsinhan Tsai,[3] Wanyi Nie,[3] Binghao Wang,[1] Claudine Katan,[2] Ram Seshadri,[4,5,6] Aditya D. Mohite,[3] Jacky Even,[7] Tobin J. Marks,[1] Mercouri G. Kanatzidis[1]*

[1]Department of Chemistry and Argonne-Northwestern Solar Energy Research Center, Northwestern University, Evanston, Illinois 60208, USA

[2] Institut des Sciences Chimiques de Rennes (ISCR), UMR 6226, CNRS - Université de Rennes 1 - Ecole Nationale Supérieure de Chimie de Rennes - INSA Rennes, France

[3]Los Alamos National Laboratory, Los Alamos, NM 87545, USA

[4]Materials Research Laboratory, University of California, Santa Barbara, California 93106, USA

[5]Materials Department, University of California, Santa Barbara, California 93106, USA

[6]Department of Chemistry and Biochemistry, University of California, Santa Barbara, California 93106, USA

[7]Fonctions Optiques pour les Technologies de l'Information (FOTON), UMR 6082, CNRS - INSA Rennes - Université de Rennes 1, France

*Corresponding authors. E-mail: m-kanatzidis@northwestern.edu

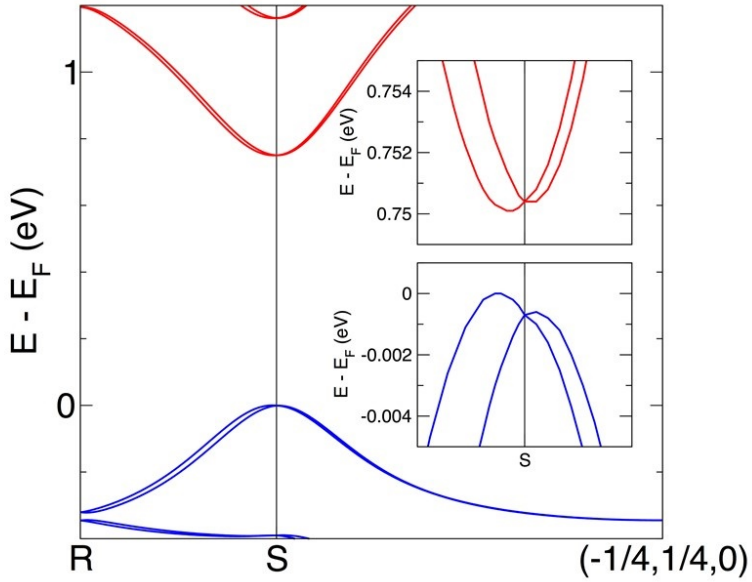

Figure S1. Closeup view of the electronic band structure of the n = 2 member of the $(GA)(MA)_nPb_nI_{3n+1}$ ACI perovskites, highlighting the Rashba splitting of the valence and conduction band extrema around the S point of the Brillouin zone.

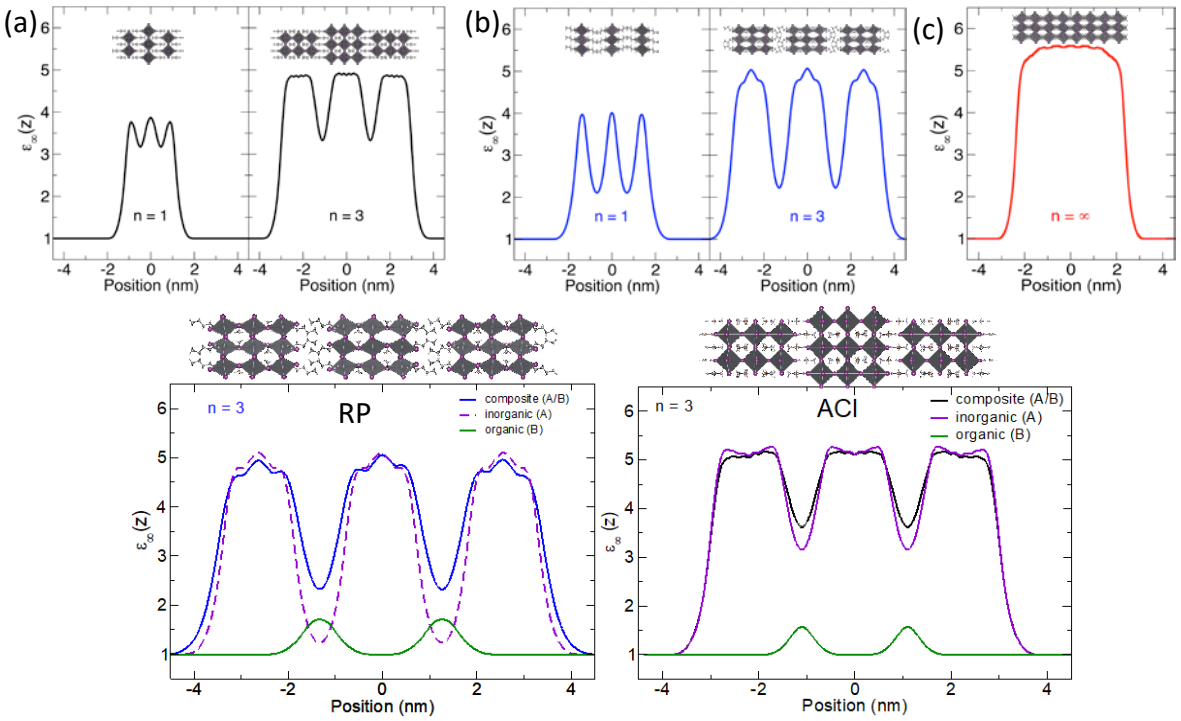

Figure S2. Dielectric profiles for (a) $(GA)(MA)_nPb_nI_{3n+1}$, (b) $(BA)_2(MA)_{n-1}Pb_nI_{3n+1}$ for n = 1 and n = 3. (c) Dielectric profile for bulk 3D $MAPbI_3$. (d) Comparison between the dielectric profiles of RP and ACI layered perovskites with the same n-member, illustrating the net contribution of the spacer cations to the dielectric profile (green trace).

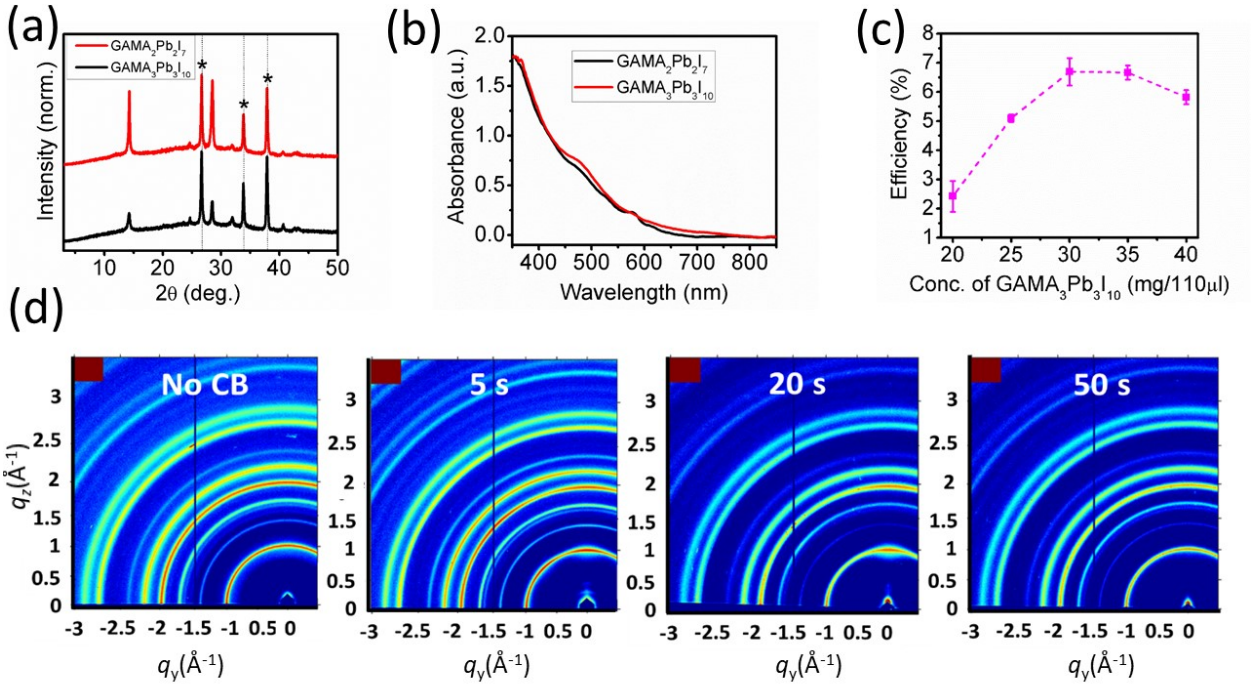

Figure S3. (a) PXRD patterns of thin films of $(GA)(MA)_2Pb_2I_7$ and $(GA)(MA)_3Pb_3I_{10}$ obtained from the chlorobenzene (CB) anti-solvent method. (b) Optical absorption spectra of thin films of $(GA)(MA)_2Pb_2I_7$ and $(GA)(MA)_3Pb_3I_{10}$ obtained from the anti-solvent method. (c) Efficiency vs. precursor solution concentration for devices made of $(GA)(MA)_3Pb_3I_{10}$ using the anti-solvent method. (d) GIWAXS patterns of thin films of $(GA)(MA)_3Pb_3I_{10}$ as a function of the delay in dripping time of the anti-solvent.

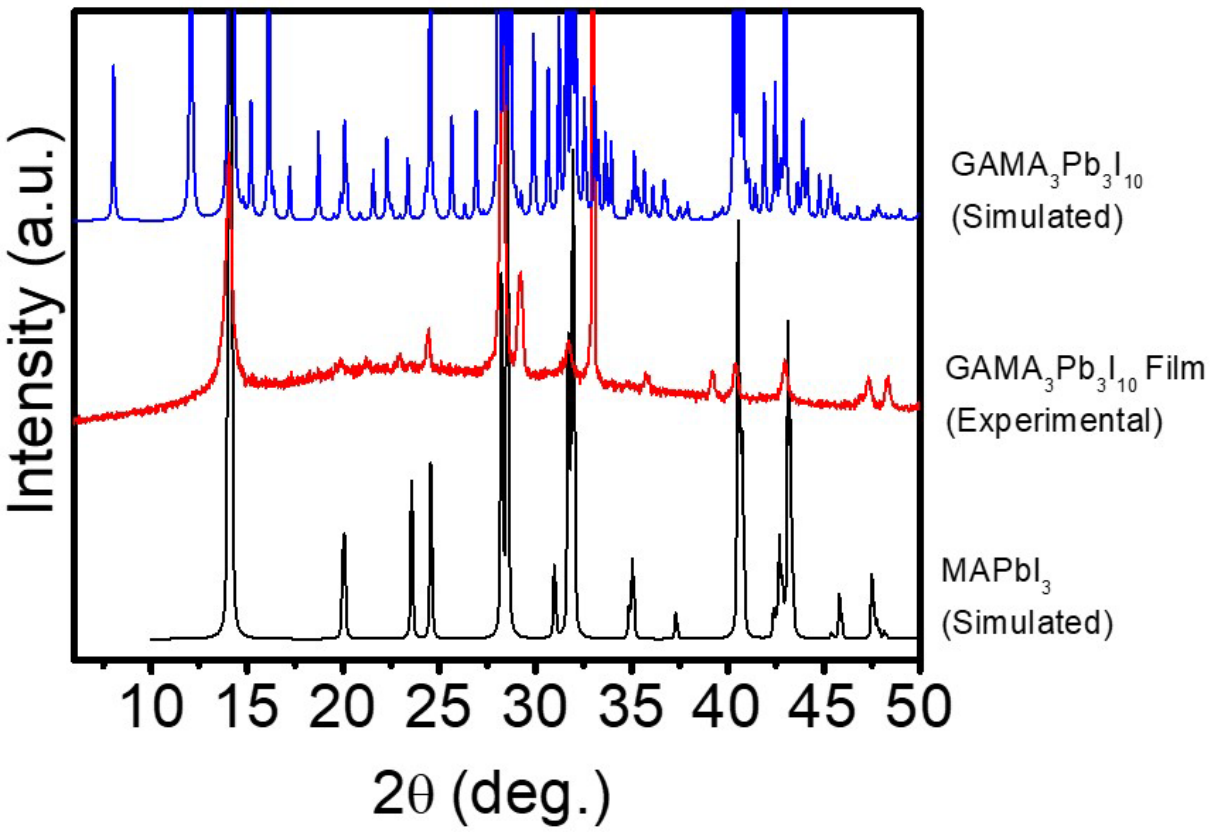

Figure S4. Close up view of the PXRD pattern of a thin film of $(GA)(MA)_3Pb_3I_{10}$ obtained from the anti-solvent method, referenced against the calculated patterns of $(GA)(MA)_3Pb_3I_{10}$ and $MAPbI_3$, highlighting the formation of the 2D ACI perovskite on the substrate.

Table S1. Atomic coordinates ($x10^4$) and equivalent isotropic displacement parameters ($Å^2x10^3$) for $GAMAPbI_4$ at 293 K with estimated standard deviations in parentheses.

Label	x	y	z	Occupancy	U_{eq}*
Pb(1)	0	0	0	1	32(1)
I(1)	0	418(2)	1667(2)	1	66(1)
I(2)	5000	0	0	1	69(2)
I(3)	0	7500	306(2)	1	78(2)
N(1)	5000	2500	1110(50)	1	220(30)
N(2)	0	7500	2231(15)	1	54(5)
N(3)	0	8461(14)	3279(13)	1	54(5)
C(1)	5000	2500	1910(50)	1	220(30)
C(2)	0	7500	2948(15)	1	54(5)
H(1n3)	0	8490.85	3740.93	1	64.8
H(2n3)	0	9050.08	3031.18	1	64.8
H(1n2)	0	6895.2	1999.53	1	64.8
H(2n2)	0	8104.8	1999.53	1	64.8
H(1n1)	5930.53	2950.49	956.76	0.25	265.7
H(2n1)	5290.76	1858.9	956.76	0.25	265.7
H(3n1)	3778.71	2690.61	956.76	0.25	265.7
H(1c1)	6221.29	2309.39	2061.62	0.25	265.7
H(2c1)	4709.24	3141.1	2061.62	0.25	265.7
H(3c1)	4069.47	2049.51	2061.62	0.25	265.7

*U_{eq} is defined as one third of the trace of the orthogonalized U_{ij} tensor.

Table S2. Atomic coordinates ($x10^4$) and equivalent isotropic displacement parameters ($Å^2x10^3$) for $GAMA_2Pb_2I_7$ at 293 K with estimated standard deviations in parentheses.

Label	x	y	z	Occupancy	U_{eq}^*
Pb(1)	5000	2486(2)	3875(1)	1	32(2)
Pb(2)	5000	2486(2)	1826(1)	1	33(2)
I(1)	5000	0	4052(3)	1	83(5)
I(2)	5000	5000	2009(4)	1	82(4)
I(3)	5000	2889(7)	852(2)	1	69(3)
I(4)	5000	2175(3)	2840(3)	1	84(2)
I(5)	5000	2900(6)	4856(2)	1	67(3)
I(6)	0	2516(10)	3822(3)	1	72(3)
I(7)	0	2473(10)	1825(3)	1	75(3)
I(8)	5000	5000	3742(4)	1	119(7)
I(9)	5000	0	1696(3)	1	109(7)
N(1)	0	0	2786(17)	1	103(19)
N(2)	0	5000	2587(1)	1	500(100)
N(3)	0	5000	1276(13)	1	65(14)
N(4)	5000	5000	-260(30)	1	190(40)
N(5)	5000	932(1)	-180(20)	1	140(30)
N(6)	5000	0	460(20)	1	140(30)
N(7)	5000	986(12)	5810(11)	1	33(7)
N(8)	5000	0	5208(10)	1	33(7)
C(1)	0	0	3264(17)	1	103(19)
C(2)	0	5000	3065(1)	1	500(100)
C(3)	0	5000	798(13)	1	65(14)
C(4)	5000	5000	220(30)	1	190(40)
C(5)	5000	0	30(20)	1	140(30)
C(6)	5000	0	5638(10)	1	33(7)
H(1n1)	873.54	480.25	2693.79	0.25	123.3
H(2n1)	381.84	-624.48	2693.79	0.25	123.3
H(3n1)	-1255.38	144.23	2693.79	0.25	123.3
H(1n2)	1277.74	4921.35	2494.7	0.25	596.4
H(2n2)	-772.93	4477.13	2494.7	0.25	596.4
H(3n2)	-504.8	5601.52	2494.7	0.25	596.4
H(1n3)	-1011.97	4595.94	1368.49	0.25	78.5
H(2n3)	1194.73	4756.77	1368.49	0.25	78.5

H(3n3)	-182.76	5647.29	1368.49	0.25	78.5
H(1n4)	3758.24	4828	-351.94	0.25	229.2
H(2n4)	5327.7	5632.37	-351.94	0.25	229.2
H(3n4)	5914.06	4539.63	-351.94	0.25	229.2
H(1n5)	5000	932.01	-461.06	1	167.6
H(2n5)	5000	1532.67	-45.14	1	167.6
H(1n6)	5000	-600.66	600.24	0.5	167.6
H(2n6)	5000	600.66	600.24	0.5	167.6
H(1n7)	5000	1064.18	6085.52	1	39.8
H(2n7)	5000	1544.4	5645.3	1	39.8
H(1n8)	5000	-600.66	5069.11	0.5	39.8
H(2n8)	5000	600.66	5069.11	0.5	39.8
H(1c1)	966.4	-528.76	3366.27	0.25	123.3
H(2c1)	418.1	689.59	3366.27	0.25	123.3
H(3c1)	-1384.5	-160.83	3366.27	0.25	123.3
H(1c2)	1416.32	4946.5	3167.17	0.25	596.4
H(2c2)	-616.97	5649.92	3167.17	0.25	596.4
H(3c2)	-799.35	4403.58	3167.17	0.25	596.4
H(1c3)	846.04	5579.56	696.02	0.25	78.5
H(2c3)	564.88	4337.96	696.02	0.25	78.5
H(3c3)	-1410.92	5082.47	696.02	0.25	78.5
H(1c4)	4707.54	4293.9	320.55	0.25	229.2
H(2c4)	6349.82	5224.37	320.55	0.25	229.2
H(3c4)	3942.64	5481.73	320.55	0.25	229.2

*U_{eq} is defined as one third of the trace of the orthogonalized U_{ij} tensor.

Table S3. Atomic coordinates ($x10^4$) and equivalent isotropic displacement parameters ($Å^2x10^3$) for $GAMA_3Pb_3I_{10}$ at 293 K with estimated standard deviations in parentheses.

Label	x	y	z	Occupancy	U_{eq}*
Pb(1)	0	0	0	1	35(1)
Pb(2)	0	12(1)	1451(1)	1	33(1)
I(1)	0	5406(2)	2144(1)	1	74(1)
I(2)	0	7500	1335(1)	1	84(2)
I(3)	5000	0(3)	1427(1)	1	80(1)
I(4)	0	2500	1558(1)	1	88(2)
I(5)	0	283(2)	713(1)	1	91(2)
I(6)	5000	0	0	1	128(2)
I(7)	0	7500	77(2)	1	151(3)
N(1)	5000	7500	953(1)	1	530(90)
N(2)	-5000	2500	839(18)	1	230(30)
N(3)	0	7500	3166(19)	1	190(20)
N(4)	5000	2500	2614(7)	1	60(5)
N(5)	5000	1541(14)	2163(6)	1	60(5)
C(1)	5000	7500	612(1)	1	530(90)
C(2)	-5000	2500	498(18)	1	230(30)
C(3)	0	7500	2825(19)	1	190(20)
C(4)	5000	2500	2306(7)	1	60(5)
H(1n1)	6282.98	7574.81	1019.02	0.25	633.3
H(2n1)	4231.65	8030.03	1019.02	0.25	633.3
H(3n1)	4485.37	6895.16	1019.02	0.25	633.3
H(1n2)	-6285.59	2437.95	905.09	0.25	273.8
H(2n2)	-4251.98	1962.44	905.09	0.25	273.8
H(3n2)	-4462.43	3099.62	905.09	0.25	273.8
H(1n3)	-1285.48	7562.63	3232	0.25	222.8
H(2n3)	536.54	6900.14	3232	0.25	222.8
H(3n3)	748.94	8037.23	3232	0.25	222.8
H(1n4)	5000	3105.77	2712.43	0.5	72.3
H(2n4)	5000	1894.23	2712.43	0.5	72.3
H(1n5)	5000	1514.89	1965.17	1	72.3
H(2n5)	5000	948.27	2268.09	1	72.3
H(1c1)	3886.23	7953.88	539.15	0.25	633.3
H(2c1)	4787.21	6780.46	539.15	0.25	633.3

H(3c1)	6326.56	7765.66	539.15	0.25	633.3
H(1c2)	-6200.48	2107.99	425.22	0.25	273.8
H(2c2)	-3735.01	2165.06	425.22	0.25	273.8
H(3c2)	-5064.51	3226.95	425.22	0.25	273.8
H(1c3)	98.44	6774.04	2752.13	0.25	222.8
H(2c3)	1181.83	7906.52	2752.13	0.25	222.8
H(3c3)	-1280.27	7819.44	2752.13	0.25	222.8

*U_{eq} is defined as one third of the trace of the orthogonalized U_{ij} tensor.

Table S4. Anisotropic displacement parameters ($Å^2x10^3$) for $GAMAPbI_4$ at 293 K with estimated standard deviations in parentheses.

Label	U_{11}	U_{22}	U_{33}	U_{12}	U_{13}	U_{23}
Pb(1)	25(1)	28(1)	42(1)	0	0	3(1)
I(1)	90(2)	63(2)	44(2)	0	0	-2(2)
I(2)	21(2)	111(3)	74(2)	0	0	21(2)
I(3)	155(4)	22(2)	57(2)	0	0	0

The anisotropic displacement factor exponent takes the form: $-2\pi^2[h^2a^{*2}U_{11} + ... + 2hka^*b^*U_{12}]$.

Table S5. Anisotropic displacement parameters ($Å^2x10^3$) for $GAMA_2Pb_2I_7$ at 293 K with estimated standard deviations in parentheses.

Label	U_{11}	U_{22}	U_{33}	U_{12}	U_{13}	U_{23}
Pb(1)	24(2)	26(3)	47(2)	0	0	1(2)
Pb(2)	37(2)	28(3)	34(2)	0	0	0(2)
I(1)	139(12)	35(5)	74(6)	0	0	0
I(2)	102(9)	40(6)	103(7)	0	0	0
I(3)	97(7)	75(5)	36(3)	0	0	34(2)
I(4)	107(3)	119(3)	26(2)	0	0	-20(4)
I(5)	91(7)	67(4)	43(3)	0	0	20(2)
I(6)	18(3)	128(8)	72(4)	0	0	12(4)
I(7)	26(3)	125(8)	72(3)	0	0	-25(4)
I(8)	233(17)	6(4)	119(8)	0	0	0
I(9)	248(19)	13(5)	65(5)	0	0	0

The anisotropic displacement factor exponent takes the form: $-2\pi^2[h^2a^{*2}U_{11} + ... + 2hka^*b^*U_{12}]$.

Table S6. Anisotropic displacement parameters ($Å^2x10^3$) for $GAMA_3Pb_3I_{10}$ at 293 K with estimated standard deviations in parentheses.

Label	U_{11}	U_{22}	U_{33}	U_{12}	U_{13}	U_{23}
Pb(1)	37(1)	34(1)	35(1)	0	0	2(1)
Pb(2)	31(1)	29(1)	38(1)	0	0	0(1)
I(1)	116(2)	72(2)	35(2)	0	0	-10(1)
I(2)	130(4)	25(2)	99(3)	0	0	0
I(3)	26(1)	123(2)	90(2)	0	0	-15(2)
I(4)	172(4)	25(2)	68(3)	0	0	0
I(5)	120(2)	128(2)	26(2)	0	0	-2(2)
I(6)	25(2)	250(5)	108(4)	0	0	-1(5)
I(7)	304(8)	21(2)	128(5)	0	0	0

The anisotropic displacement factor exponent takes the form: $-2\pi^2[h^2a^{*2}U_{11} + ... + 2hka^*b^*U_{12}]$.

Table S7. Calculated band dispersion (meV) along the perovskite layer stacking direction in reciprocal space for ACI (GA)$(MA)_nPb_nI_{3n+1}$ perovskites with n = 1-3.

n-member	**1**	**2**	**3**
k-direction	W-T	Γ-Y	W-T
VBM (meV)	48	63	< 1
CBM (meV)	11	26	4